scientific reports

Check for updates

OPEN

Optimized Zn substituted $CoFe_2O_4$ nanoparticles for high efficiency magnetic hyperthermia in biomedical applications

Ali Aftabi[1,2]✉, Asra Babakhani[1] & Rohollah Khoshlahni[3]

This study presents a systematic study on the structural, magnetic, and hyperthermia properties of Zn-substituted cobalt ferrite ($Zn_xCo_{1-x}Fe_2O_4$, x = 0.0–0.7) nanoparticles synthesized via the hydrothermal method. X-ray diffraction patterns confirmed a pure spinel structure, with Rietveld refinement revealing cation redistribution and lattice distortions. Magnetic measurements showed a transition from ferrimagnetic (x ≤ 0.2) to superparamagnetic behavior (x ≥ 0.5), accompanied by a peak in saturation magnetization at x = 0.2 and a continuous decrease in coercivity. These changes were attributed to Zn-induced modulation of cation distribution and superexchange interactions. Magnetic hyperthermia studies demonstrated that $Zn_{0.6}Co_{0.4}Fe_2O_4$ exhibited the highest specific loss power (SLP) and intrinsic loss power (ILP) under alternating magnetic fields (65–125 Oe) and frequencies (250–350 kHz). The observed quadratic dependence of SLP on field amplitude confirmed adherence to linear response theory, with experimental conditions remaining within clinical safety limits. These findings highlight $Zn_{0.6}Co_{0.4}Fe_2O_4$ as an efficient candidate for magnetic hyperthermia applications, demonstrating tunable structural and magnetic properties for biomedical use.

Keywords Magnetic hyperthermia, Nanoparticles, Spinel ferrite, Cation distribution

In 2025, an estimated 9.7 million people globally are expected to die from cancer, with projections suggesting this figure could exceed 13 million by 2030 [1,2]. Early detection, precise diagnosis, and effective treatments are essential for improving survival rates. As a result, recent decades have seen substantial efforts to advance new diagnostic tools and therapies[3–6]. Magnetic nanostructures have attracted considerable interest recently due to their potential medical diagnosis and treatment applications[7–15]. These nanoparticles, typically smaller than 100 nm and made from magnetic materials like Fe_3O_4 and $CoFe_2O_4$, exhibit unique magnetic properties like superparamagnetism and high saturation magnetization[16,17]. These characteristics make them well-suited for biomedical applications, including magnetic particle imaging (MPI), magnetic resonance imaging (MRI), biosensing, diagnostic, targeted drug delivery, and cell separation and purification[17–19]. Moreover, magnetic nanoparticles are being actively explored for their potential in hyperthermia therapy. Magnetic hyperthermia refers to the phenomenon in which magnetic nanoparticles generate heat when subjected to an alternating magnetic field. In magnetic hyperthermia therapy, nanoparticles dispersed in a biocompatible carrier fluid (typically water) generate localized heat when subjected to a radiofrequency magnetic field. Tumor cells exhibit a greater sensitivity to heat than healthy cells, so raising the temperature to 42–46 °C selectively damages cancerous tissues while leaving healthy parts unharmed. This approach has demonstrated encouraging outcomes in preclinical studies and is now undergoing evaluation in clinical trials[17,20,21].

In magnetic hyperthermia, heat generation by magnetic nanoparticles arises from their capability to convert magnetic energy into heat. Several mechanisms contribute to heat production when these nanoparticles are subjected to an alternating magnetic field. These include hysteresis losses (in cases where the nanoparticle's coercive field is non-zero), eddy currents (if the nanoparticles are conductive), Néel relaxation (oscillation of magnetic moments within the nanoparticles), and Brownian relaxation (physical rotation of the entire nanoparticle)[22–25].

The efficiency of magnetic material in hyperthermia is generally assessed through its specific loss power (SLP), which refers to the produced power per unit mass of the nanoparticles. According to linear response

[1]Department of Physics, Faculty of Science, University of Kurdistan, Sanandaj 66177-15175, Iran. [2]Research Center for Nanotechnology, University of Kurdistan, Sanandaj 66177-15175, Iran. [3]School of Physics, Institute for Research in Fundamental Sciences (IPM), Tehran 19395-5531, Iran. ✉email: a.aftabi@uok.ac.ir

theory, SLP depends on both the properties of the nanoparticles (such as shape, particle size, relaxation times, anisotropy, magnetic susceptibility, saturation magnetization, concentration, volume, and the viscosity of the surrounding liquid) and the experimental conditions (including the amplitude, frequency, and waveform of the alternating magnetic field)[2,26–28].

However, applying magnetic fields is subject to limitations because of non-specific heating brought on by tissues' generated eddy currents. To avoid patient discomfort, a threshold exists for the product of field amplitude and frequency, initially set as $H_0 f \leq 4.85 \times 10^8$ A·m^{-1}·s^{-1} (6.1×10^6 Oe·Hz)[29]. Later, Hergt et al. adjusted this limit to $H_0 f \leq 5 \times 10^9$ A·m^{-1}·s^{-1} (6.3×10^7 Oe·Hz) for smaller body parts[30]. Hence, optimizing the intrinsic properties of magnetic nanoparticles to enhance their SLP while complying with these constraints is crucial. Magnetic nanoparticles with high SLP are favored for hyperthermia therapy because they can achieve therapeutic heating with lower concentrations in a shorter period.

Among various magnetic materials explored for biomedical applications, such as magnetic hyperthermia, spinel ferrite nanoparticles are viral. These materials have a general formula of MFe_2O_4, M represents a divalent transition metal (e.g., Mn, Cu, Ni, Zn, Co, Fe), and they possess a face-centered cubic (FCC) crystal structure[31,32]. Every unit cell comprises 8 formula units[33]. The spinel structure has two types of interstitial sites, A and B. These sites are inhabited by metal cations coordinated by oxygen in octahedral (B) and tetrahedral (A) configurations. For a standard spinel structure, tetrahedral sites are occupied by divalent M^{2+} cations, while Fe^{3+} cations are situated in octahedral sites, yielding the structure $(M^{2+})_A[Fe^{3+}]_BO_4$ [34–36]. Inverse spinel structures, M^{2+} cations are located in octahedral sites, while the Fe^{3+} ions are distributed in tetrahedral and octahedral positions, with half in each, resulting in the structure $(Fe^{3+})_A[M^{2+}Fe^{3+}]_BO_4$ [31,37]. A mixed spinel configuration, where both M^{2+} and Fe^{3+} ions occupy tetrahedral and octahedral sites, is expressed as $(M_{1-\gamma}Fe^{3+}{}_\gamma)_A[M^{2+}{}_\gamma Fe^{3+}{}_{2-\gamma}]_BO_4$ [38]. The distribution sites, quantified by the inversion degree (δ), which is the Fe^{3+} ratio in tetrahedral versus octahedral sites ($\delta = Fe_{tetra}/Fe_{octa}$), heavily influence the magnetic, optical, electrical, and structural characteristics of mixed spinel ferrites[39,40]. Parameters like cation substitution, concentration, and synthesis method affect this cation distribution[31,41].

Cobalt ferrite ($CoFe_2O_4$) is a well-researched spinel ferrite with outstanding magnetic and structural properties, making it highly suitable for biomedical uses, particularly magnetic hyperthermia therapy[17]. With high saturation magnetization and robust magnetocrystalline anisotropy, $CoFe_2O_4$ is highly responsive to alternating magnetic fields, facilitating effective heat generation in hyperthermia applications[17,42]. Its relatively high Curie temperature further ensures thermal stability in physiological conditions, a critical requirement for sustained therapeutic use of magnetic nanoparticles[43]. The spinel structure of $CoFe_2O_4$ allows for flexible cation distribution among tetrahedral and octahedral sublattices, enabling precise tuning of its magnetic and hyperthermic properties through cation substitution. Extensive research has focused on tailoring $CoFe_2O_4$'s intrinsic properties via strategies such as synthesis modification or doping with other transition metal cations[44–48].

Furthermore, the biocompatibility and potential cytotoxicity of $CoFe_2O_4$ nanoparticles are crucial considerations for their biomedical applications, including magnetic hyperthermia. Various factors, such as particle size, surface charge, and surface modifications, significantly influence their interactions with biological systems[49]. Studies have shown that uncoated $CoFe_2O_4$ nanoparticles may exhibit cytotoxic effects, primarily due to their physicochemical properties[50]. Smaller nanoparticles, with their increased surface area, tend to exhibit higher reactivity, potentially leading to increased toxicity. However, appropriate surface functionalization can mitigate these effects. Coating $CoFe_2O_4$ nanoparticles with biocompatible materials, such as citric acid or polyethylene glycol (PEG), has been demonstrated to enhance their stability in biological environments and reduce cytotoxicity[49–51]. Additionally, the substitution of transition metals within the cobalt ferrite structure can improve biocompatibility[52]. Research on transition metal-substituted $CoFe_2O_4$ nanoparticles, including those with zinc substitution, indicates that such modifications can reduce toxicity and enhance their biocompatibility, making them more suitable for biomedical applications[50].

In this study, Zinc (Zn) was chosen for substitution due to its distinctive effect on cation distribution within the $CoFe_2O_4$ lattice, reducing toxicity and improving biocompatibility. As a diamagnetic ion with no magnetic moment, Zn^{2+} preferentially occupies tetrahedral sites, contrasting with Co^{2+} ions. This substitution alters the magnetic interactions between octahedral and tetrahedral sublattices by redistributing cations, which affects superexchange interactions. This redistribution may enhance saturation magnetization while decreasing magnetic anisotropy, both of which can significantly influence the specific loss power (SLP) of nanoparticles, a critical gauge of their hyperthermia effectiveness. By varying Zn content, this study investigates how structural and magnetic properties can be systematically engineered to optimize $CoFe_2O_4$'s performance for magnetic hyperthermia, aiming for efficient and controlled heating at biocompatible magnetic field strengths.

Experimental methods

Synthesis

To examine how Zn substitution affects cobalt ferrite's structural, magnetic, and magnetic hyperthermia characteristics, $Zn_xCo_{1-x}Fe_2O_4$ (x = 0.0, 0.2, 0.5, 0.6, and 0.7) nanoparticles were produced using a hydrothermal technique. To create a 1 M precursor solution, 20 mL of double-distilled water was mixed with stoichiometric quantities of zinc nitrate ($Zn(NO_3)_2{\cdot}6\,H_2O$), cobalt nitrate ($Co(NO_3)_2{\cdot}6\,H_2O$), and iron nitrate ($Fe(NO_3)_3{\cdot}9\,H_2O$). The solution was then continuously agitated with a magnetic stirrer for an hour. During this period, 10 mL of a 3 M sodium hydroxide (NaOH) solution was added drop by drop to initiate the precipitation reaction. the resultant mixture was put into a 50 mL Teflon-lined stainless-steel autoclave with a 60% filling capacity. After that, the autoclave was sealed and baked for 18 h at 200 °C. After cooling, the precipitate obtained was removed from the autoclave, washed several times with double-distilled water to remove any residual ions, and dispersed using an ultrasonic bath to ensure complete removal of unreacted materials. Following washing, a stable colloidal solution was prepared by dispersing 1.5 mg/mL of the synthesized nanoparticles in double-distilled water. This

solution was subjected to ultrasonication for 10 min, yielding a stable dispersion that did not settle even after several weeks.

Characterization

The phase purity and structural characteristics of the synthesized $Zn_xCo_{1-x}Fe_2O_4$ (x = 0.0, 0.2, 0.5, 0.6, and 0.7) nanoparticle samples have been analyzed using X-ray diffraction (XRD) on an Explorer diffractometer with Cu Kα radiation (λ = 1.54060 Å). XRD patterns were used to confirm the desired spinel structure's formation and assess the crystallographic changes induced by Zn substitution. Field-emission scanning electron microscopy (FESEM) was conducted to examine the samples' grain morphology and microstructural properties. FESEM images provided insights into particle size, shape, and surface characteristics, which are crucial for understanding the impact of Zn substitution on the physical morphology of the nanoparticles. The magnetic properties of the prepared nanoparticles were characterized by a vibrating sample magnetometer (VSM). Magnetic hysteresis loops were recorded to determine key parameters including saturation magnetization (Ms), coercivity (Hc), and effective anisotropy constant (K_{eff}), which are essential for evaluating the magnetic behavior of Zn-substituted cobalt ferrite. For magnetic hyperthermia characterization, the heating potential of each sample was investigated using an AC magnetic induction heating system under various field strengths and frequencies. This assessment allowed for the determination of hyperthermic efficiency, which is relevant for potential biomedical applications, including magnetic hyperthermia therapy.

Results and discussion

XRD analysis and cation distribution

The X-ray diffraction (XRD) patterns of the prepared $Zn_xCo_{1-x}Fe_2O_4$ (x = 0.0, 0.2, 0.5, 0.6, and 0.7) nanoparticles were recorded at room temperature. The recorded patterns are presented in Fig. 1a–e. The prominent diffraction peaks centered around 2θ ~ 18.3°, 30.2°, 35.5°, 43.2°, 53.6°, 57.2°, and 62.7°, correspond to the reflection planes (111), (220), (311), (400), (422), (511), and (440), clearly indicates the formation of spinel structures with $Fd\bar{3}m$ space group for all prepared samples. The obtained XRD patterns match the JCPDS card numbers of $CoFe_2O_4$ (No. 156–5326) and $ZnFe_2O_4$ (No. 156–7173). The patterns do not indicate any additional phase which confirms high-purity crystalline powder forming for all samples. To determine the structural and microstructural parameters, such as atom's coordinates, cations site occupancy, thermal parameters, lattice parameters, micro-strain, and crystallite size, the Rietveld refinement has been performed using FollProf Suite software. The Rietveld refinement diffraction patterns, for various prepared nanoparticles, are shown in Fig. 1a–e. Red circles demonstrate experimental data (I_{obs}), continuing black lines show the calculated patterns (I_{cal}), green vertical lines display the Bragg peaks positions for the $Fd\bar{3}m$ space group, and blue lines depict the discrepancy between the measured and estimated diffraction patterns (I_{obs}- I_{cal}). The fitting quality of the diffraction patterns is determined by the fit goodness parameter (χ^2) and various R-factors such as R_{Bragg} (Bragg factor), R_{exp}(expected profile factor), R_{wp} (weighted profile factor), R_p (Profile factor). The values obtained for these factors across different samples are recorded in the Fig. 1a–e insets. The low values obtained for the fit goodness parameter and various R factors indicate that the refined patterns align well with the experimental data. The refined values of atomic coordinates, cation site occupancy, lattice parameter, and unit cell volume for various prepared nanoparticles are presented in Tables 1 and 2. For the $Zn_xCo_{1-x}Fe_2O_4$ samples, as shown in Table 1, the $Zn^{2+}{}_{II}$, $Co^{2+}{}_{II}$, $Fe^{3+}{}_{II}$ cations occupying the Wyckoff 16(*d*) positions at (1/2,1/2,1/2), the $Zn^{2+}{}_{I}$, $Co^{2+}{}_{I}$, and $Fe^{3+}{}_{I}$ cations occupying the Wyckoff 8(*a*) positions at (1/8,1/8,1/8) and O^{2-} anions occupying Wyckoff 32(*e*) sites at (*u*, *u u*)[24,53,54]. Cation site occupancies and oxygen position (x = y = z = u) were free parameters during the refinement. u is considered an indicator of lattice distortion in the spinel structure. In a perfect lattice without distortion, u typically has a value of 0.2500. The refined quantities for the prepared samples range from 0.2492 to 0.2538. The obtained values reflect a minor distortion in the spinel lattice, which is typically anticipated in real systems due to the unavoidable presence of structural imperfections[24]. The standard ionic radius of the Co^{2+} cation is 0.58 Å in fourfold coordination and 0.75 Å in sixfold coordination, while for the Zn^{2+} cation, it is 0.60 Å and 0.74 Å, respectively. Therefore, the redistribution of cations due to Zn substitution is expected to alter the radii of the octahedral and tetrahedral sites, allowing the lattice structure to adjust for optimal stability by minimizing potential energy. Consequently, oxygen anions will likely shift toward or away from the neighboring A- or B-site cations along the [111] direction. This adjustment could result in a reciprocal change in the sizes of the octahedral and tetrahedral sites, ultimately affecting the oxygen positional parameter[24,55].

As shown in Table 2, the lattice constant (a = b = c) and the volume of the unit cell (V) enhance with the rise in the Zn doping level. The enhancement of the lattice constant is attributed to the greater ionic radius of Zn^{2+} (~ 0.60 Å) compared to Co^{2+} (~ 0.58 Å). Using the estimated unit cell volume, the X-ray density ρ of the prepared nanoparticles has been deduced based on the following relationship[41]:

$$\rho = \frac{nM}{VN_A} \tag{1}$$

where n represents the number of formula units present within the unit cell ($n = 8$), M corresponds to the molar mass of the $Zn_xCo_{1-x}Fe_2O_4$ samples, and N_A shows the Avogadro number (6.022×10^{23} mol^{-1}). The estimated values of ρ are reported in Table 2. The range of the estimated ρ values is 5.300 to 5.354 g/cm^3.

Hopping lengths between the magnetic cations at the tetrahedral sites (d_A) and octahedral sites (d_B) can be deduced by the lattice parameter from the following equations[24,56]:

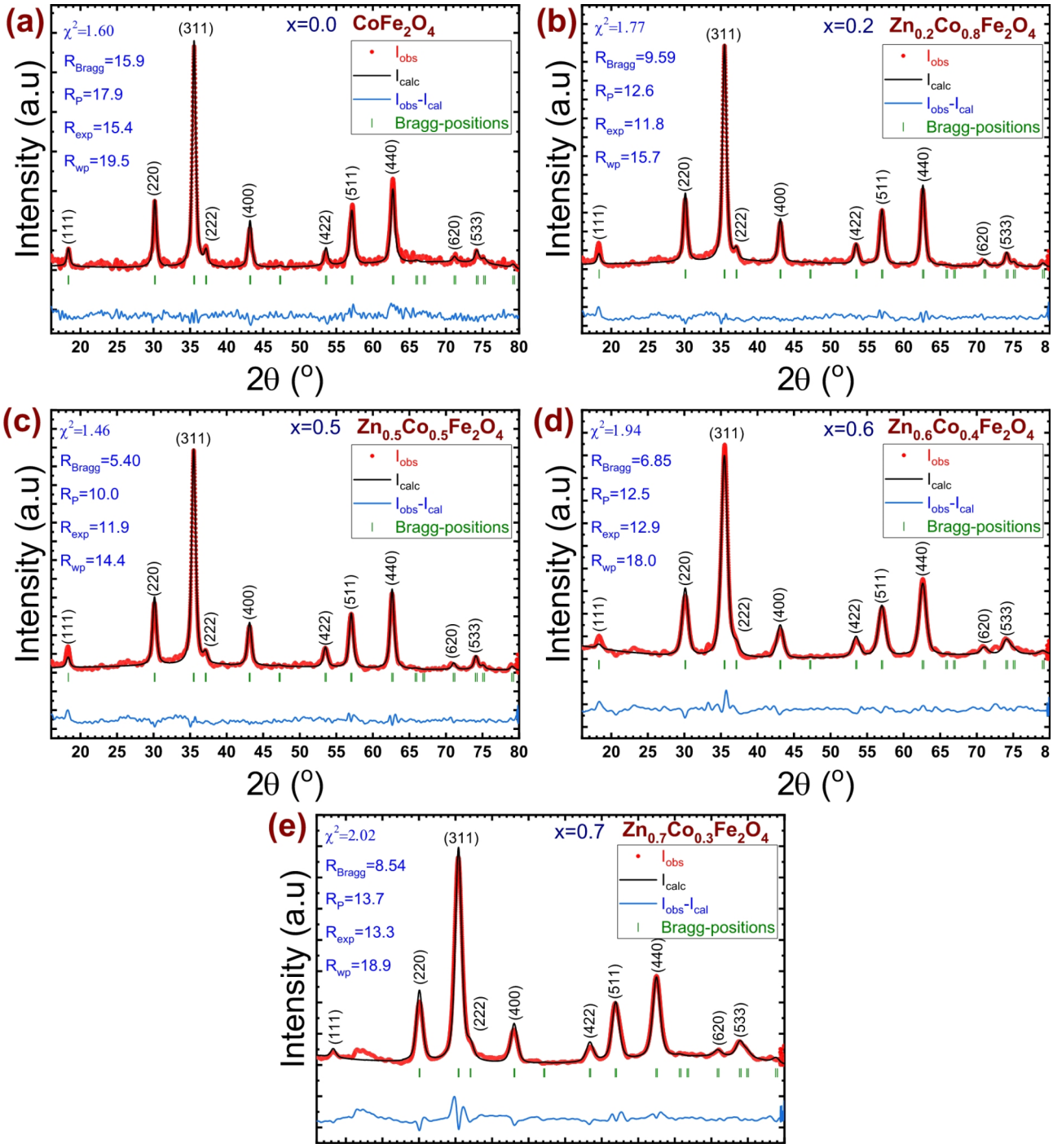

Fig. 1. XRD patterns (I_{obs}) along with Rietveld-refined fits (I_{calc}) for $Zn_xCo_{1-x}Fe_2O_4$ (x = 0.0, 0.2, 0.5, 0.6, and 0.7) samples. The discrepancy between estimated and observed data is shown by the blue line, and the green vertical bars indicate peak positions.

$$d_A = \frac{\sqrt{3}}{4}a \tag{2}$$

$$d_B = \frac{\sqrt{2}}{4}a \tag{3}$$

The calculated d_A and d_B values are reported in Table 2. The obtained d_A and d_B values show an increasing trend with the rise in the Zn doping level. The hopping length in the tetrahedral sublattice is larger than in the octahedral sublattice. It shows that the hopping probability of charge carriers among octahedral sublattices is

atoms	$CoFe_2O_4$		$Zn_{0.2}Co_{0.8}Fe_2O_4$		$Zn_{0.5}Co_{0.5}Fe_2O_4$		$Zn_{0.6}Co_{0.4}Fe_2O_4$		$Zn_{0.7}Co_{0.3}Fe_2O_4$	
	x = y = z	Occ	x = y = z	occ	x = y = z	Occ	x = y = z	Occ	x = y = z	Occ
O	0.2527	0.174	0.2515	0.183	0.2503	0.180	0.2492	0.172	0.2538	0.161
Zn_{II}			0.5000	0.006	0.5000	0.016	0.5000	0.019	0.5000	0.022
Co_{II}	0.5000	0.031	0.5000	0.025	0.5000	0.015	0.5000	0.012	0.5000	0.009
Fe_{II}	0.5000	0.052	0.5000	0.048	0.5000	0.045	0.5000	0.045	0.5000	0.044
Zn_I			0.1250	0.002	0.1250	0.006	0.1250	0.006	0.1250	0.008
Co_I	0.1250	0.011	0.1250	0.009	0.1250	0.005	0.1250	0.004	0.1250	0.003
Fe_I	0.1250	0.031	0.1250	0.032	0.1250	0.033	0.1250	0.033	0.1250	0.033

Table 1. Estimated atomic coordinates (x, y, z) and cation site occupancy (Occ) values for various samples, obtained from Rietveld refinement.

Sample	a (Å)	V (Å^3)	ρ (g/cm^3)	d_A (Å)	d_B (Å)	r_A (Å)	r_B (Å)	d_{AE} (Å)	d_{BE} (Å)	d_{BEU} (Å)	T
$CoFe_2O_4$	8.377	587.84	5.303	3.627	2.962	0.533	0.752	3.026	2.898	2.962	1.0201
$Zn_{0.2}Co_{0.8}Fe_2O_4$	8.389	590.37	5.300	3.632	2.966	0.518	0.765	3.001	2.930	2.966	1.0169
$Zn_{0.5}Co_{0.5}Fe_2O_4$	8.392	591.01	5.346	3.634	2.967	0.501	0.775	2.974	2.960	2.967	1.0143
$Zn_{0.6}Co_{0.4}Fe_2O_4$	8.395	591.64	5.354	3.635	2.968	0.486	0.785	2.949	2.987	2.968	1.0121
$Zn_{0.7}Co_{0.3}Fe_2O_4$	8.408	594.39	5.345	3.641	2.972	0.555	0.750	3.063	2.882	2.973	1.0208

Table 2. Estimated values for the lattice constant (a), unit cell volume (V), density (ρ), radii of tetrahedral (r_A) and octahedral (r_B) sites, shared edge lengths for tetrahedral (d_{AE}) and octahedral (d_{BE}) sites, unshared octahedral edge length (d_{BEU}), and tolerance factor (T).

more than that of tetrahedral sublattices. Consequently, distinct physical characteristics, particularly electrical characteristics, are anticipated to vary between octahedral and tetrahedral sublattices.

The radius of the tetrahedral (r_A) and octahedral (r_B) sites, shared tetrahedral (d_{AE}) and octahedral (d_{BE}) edge lengths, and unshared octahedral edge length (d_{BEU}) have been deduced using obtained a and u parameters according to the following equation[57]:

$$r_A = a\sqrt{3}\left(u - \frac{1}{4}\right) - R(O) \tag{4}$$

$$r_B = a\left(\frac{5}{8} - u\right) - R(O) \tag{5}$$

$$d_{AE} = a\sqrt{2}\left(2u - \frac{1}{2}\right) \tag{6}$$

$$d_{BE} = a\sqrt{2}(1 - 2u) \tag{7}$$

$$d_{BEU} = a(4u^2 - 3u + \frac{11}{16})^{\frac{1}{2}} \tag{8}$$

R(O) represents the ionic radius of oxygen anions, which is approximately 1.32 Å in spinel ferrites. It is important to note that relations (4)–(8) have been previously considered in the literature for a unit cell origin at the $\bar{4}\,3m$ symmetry on the tetrahedral site. For the current Rietveld refinement, however, the origin of the unit cell is positioned at the $\bar{3}\,m$ symmetry on an octahedral vacancy. Therefore, to apply relations (4)–(8) for a unit cell origin at $\bar{3}\,m$, the parameter u in the above relations is adjusted by replacing u with u + 1/8 [24]. The estimated values of r_A, r_B, d_{AE}, d_{BE}, and d_{BEU} are presented in Table 2. As shown, the values of r_A and d_{AE} decrease with increasing Zn doping level up to x = 0.6, after which they increase for x = 0.7. In contrast, r_B and d_{BE} increase with Zn doping up to x = 0.6 and then reduce at x = 0.7. Meanwhile, d_{BEU} displays a continuous increase as Zn doping levels rise to x = 0.7. In addition, the tolerance factor (T) was estimated using the following Eqs. 2[4,58]:

$$T = \frac{1}{\sqrt{3}}\left[\frac{r_A + R(\mathrm{O})}{r_B + R(\mathrm{O})}\right] + \frac{1}{\sqrt{2}}\left[\frac{R(\mathrm{O})}{r_A + R(\mathrm{O})}\right] \tag{9}$$

.

Estimated T quantities are reported in Table 2. The amounts obtained for the prepared samples are in the range of 1.0121–1.0208. The tolerance factor equals one for ideal spinel structures[58]. Obtained values suggest the

Sample	b (Å) (M-M)	c (Å) (M-M)	d (Å) (M-M)	e (Å) (M-M)	f (Å) (M-M)	*p* (Å) (M-O)	q (Å) (M-O)	*r* (Å) (M-O)	s (Å) (M-O)
$CoFe_2O_4$	2.9617	3.4729	3.6273	5.4410	5.1298	2.0716	1.8528	3.5479	3.6404
$Zn_{0.2}Co_{0.8}Fe_2O_4$	2.9659	3.4779	3.6325	5.4488	5.1372	2.0847	1.8381	3.5196	3.6398
$Zn_{0.5}Co_{0.5}Fe_2O_4$	2.9670	3.4791	3.6338	5.4508	5.1390	2.0955	1.8213	3.4875	3.6353
$Zn_{0.6}Co_{0.4}Fe_2O_4$	2.9681	3.4804	3.6351	5.4527	5.1409	2.1055	1.8059	3.4581	3.6313
$Zn_{0.7}Co_{0.3}Fe_2O_4$	2.9727	3.4858	3.6408	5.4612	5.1488	2.0700	1.8757	3.5917	3.6592

Table 3. The cation-cation (M-M) and cation-anion (M-O) bond distances for various samples.

Sample	θ_1 (A-O-B)	θ_2 (A-O-B)	θ_3 (B-O-B)	θ_4 (B-O-B)	θ_5 (A-O-A)
$CoFe_2O_4$	124.394	149.958	91.258	125.557	77.421
$Zn_{0.2}Co_{0.8}Fe_2O_4$	124.779	151.993	90.694	125.427	78.539
$Zn_{0.5}Co_{0.5}Fe_2O_4$	125.167	154.184	90.138	125.297	79.684
$Zn_{0.6}Co_{0.4}Fe_2O_4$	125.524	156.367	89.635	125.178	80.759
$Zn_{0.7}Co_{0.3}Fe_2O_4$	124.041	148.203	91.783	125.677	76.420

Table 4. The bond angles between ions for various samples.

sample	Tetrahedral A sites	Octahedral B sites	δ
$CoFe_2O_4$	$(Co_{0.26}Fe_{0.74})$	$[Co_{0.74}Fe_{1.26}]$	0.59
$Zn_{0.2}Co_{0.8}Fe_2O_4$	$(Zn_{0.05}Co_{0.21}Fe_{0.74})$	$[Zn_{0.15}Co_{0.59}Fe_{1.26}]$	0.59
$Zn_{0.5}Co_{0.5}Fe_2O_4$	$(Zn_{0.14}Co_{0.11}Fe_{0.75})$	$[Zn_{0.42}Co_{0.39}Fe_{1.25}]$	0.60
$Zn_{0.6}Co_{0.4}Fe_2O_4$	$(Zn_{0.14}Co_{0.09}Fe_{0.77})$	$[Zn_{0.46}Co_{0.31}Fe_{1.23}]$	0.63
$Zn_{0.7}Co_{0.3}Fe_2O_4$	$(Zn_{0.18}Co_{0.08}Fe_{0.77})$	$[Zn_{0.52}Co_{0.22}Fe_{1.23}]$	0.63

Table 5. Cation distribution and inversion degree (δ) for different prepared nanoparticles.

existence of few defects within the structure and the high quality of the prepared samples using the hydrothermal technique.

The magnetic interactions in ferrite nanoparticles, which play a key role in defining their magnetic properties, are strongly affected by the distances between ions and the angles formed between bonds. The cation-cation distances (b, c, d, e, f) are computed as $b = \frac{a\sqrt{2}}{4}$, $c = \frac{a\sqrt{11}}{8}$, $d = \frac{a\sqrt{3}}{4}$, $e = \frac{a3\sqrt{3}}{8}$, and $f = \frac{a\sqrt{6}}{4}$ [59–61]. Likewise, the cation-anion distances (p, q, r, s) can be calculated utilizing the formulas $p = a(\frac{5}{8} - u)$, $q = a\sqrt{3}(u - \frac{1}{4})$, $r = a\sqrt{11}(u - \frac{1}{4})$, and $s = a\sqrt{3}(\frac{u}{3} + \frac{1}{8})$ [59–61]. The estimated values for cation-cation and cation-anion distances are reported in Table 3. It is shown that the cation-cation distances increase, whereas the cation-anion distances decrease with increasing Zn doping concentration. This behavior can be attributed to the difference in ionic radii between Co^{2+} and Zn^{2+} ions.

With the help of obtained cation-cation and cation-anion distances, the bond angles can be calculated as $\theta_1 = arccos\left(\frac{p^2+q^2-c^2}{2pq}\right)$, $\theta_2 = arccos\left(\frac{p^2+r^2-e^2}{2pr}\right)$, $\theta_3 = arccos\left(\frac{2p^2-b^2}{2p^2}\right)$, $\theta_4 = arccos\left(\frac{p^2+s-f^2}{2ps}\right)$, and $\theta_5 = arccos\left(\frac{q^2+r^2-d^2}{2pr}\right)$ [59]. The bond angles, derived from the lattice constant and oxygen positional parameters, are presented in Table 4. The θ_1, θ_2, and θ_5 bond angles enhance with rising Zn^{2+} concentration up to 0.6, while the bond angles θ_3 and θ_4 decrease during the same concentration increase. It is widely recognized that θ_1, θ_2, and θ_5 angles pertain to A-A and A-B interactions, while θ_3 and θ_4 relate to B-B interactions[62]. The increase in bond angles θ_1, θ_2, and θ_5 with rising Zn^{2+} content suggests strengthening superexchange interactions between A-A and A-B sites. Conversely, the decline in bond angles θ_3 and θ_4 with higher Zn^{2+} levels indicates a weakening of superexchange interactions between B-B sites.

The physical properties of spinel ferrites are susceptible to cation distribution among the two sublattices, making it crucial to understand this distribution to comprehend their structural and physical characteristics. Various factors like dopant levels, preparation method, annealing atmosphere, and annealing temperature, influence cation distribution. The distribution of cations between octahedral and tetrahedral interstitial sites can be roughly estimated by analyzing their Rietveld refinement of site occupancies. The deduced cations distribution and inversion degree (δ) for all the prepared nanoparticles are listed in Table 5. The estimated distributions of Zn, Co, and Fe over 8(a) and 16(d) crystallographic sites indicate mixed spinel structure for all samples. The ratio $\delta = Fe_{Tetra}/Fe_{Octa}$ specifies the degree of inversion. The Fe_{Tetra} and Fe_{Octa} represent the Fe^{3+} cations at tetrahedral (8(a)) and octahedral (16(d)) crystallographic sites. Results indicate that the degree of inversion (δ) gradually rises as zinc doping increases.

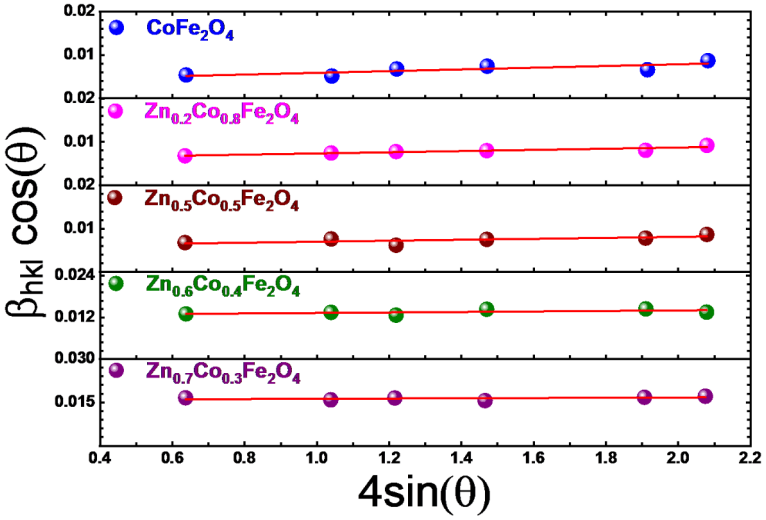

Fig. 2. Plot of βcosθ versus 4sinθ along with its linear fit for $Zn_xCo_{1-x}Fe_2O_4$ (x = 0.0, 0.2, 0.5, 0.6, and 0.7) samples.

Sample	D (nm)	ε_{ls}
$CoFe_2O_4$	35.4	0.00197
$Zn_{0.2}Co_{0.8}Fe_2O_4$	23.2	0.00136
$Zn_{0.5}Co_{0.5}Fe_2O_4$	23.7	0.00114
$Zn_{0.6}Co_{0.4}Fe_2O_4$	11.1	0.00073
$Zn_{0.7}Co_{0.3}Fe_2O_4$	8.7	0.00045

Table 6. The deduced quantities for average crystallite size (D) and microstrain (ε_{ls}) in different samples.

Nanomaterials exhibit unique properties distinct from their bulk equivalents, with surface or interface strains playing a crucial role across numerous fields. When subjected to tension or compression, materials at the nanoscale can alter their lattice constants, leading to changes in bond lengths and electron energy levels. Grain size and micro-strain generated during these processes are indicated by the full-width at half-maximum (FWHM) of the powder XRD peaks, measured in radians. Based on the Williamson-Hall equation, the integral peak width β is expressed as[63–66]:

$$\beta = \frac{K\lambda}{Dcos\theta} + 4\epsilon_{ls}tan\theta \tag{10}$$

where λ shows X-ray wavelength (Cu K_α radiation (1.54 Å)), K shows the correction factor taken as 0.94 for nanoparticles, D represents the average crystallite size, ε_{ls} stands for the microstrain, and θ is the diffraction angle. This equation can be simplified as

$$\beta\, cos\theta = \frac{K\lambda}{D} + \epsilon_{ls}\,(4sin\theta) \tag{11}$$

This equation demonstrates the linear relationship between βcosθ and 4sinθ. The full-width at half-maximum (β) of the main peaks in the XRD patterns of various samples was obtained by fitting the peaks using a pseudo-Voigt function. Instrumental broadening, referenced from a standard Al_2O_3 sample, was subtracted from each peak. Figure 2 presents the βcosθ versus 4sinθ plot and its linear fit for the different samples. The average crystallite size (D) and microstrain (ε_{ls}) for the samples were calculated from the intercept (Kλ/D) and the slope of the fitted line, respectively. As shown in Table 6, the average crystallite size (D) and strain (ε_{ls}) decrease with increasing Zn doping levels. As Zn substitution increased, ε_{ls} decreased, which correlated with an increase in crystallite size. This indicates that Zn doping reduced internal lattice distortions, allowing for more stable crystal growth. The strain relaxation likely results from the redistribution of cations within the spinel lattice, minimizing internal stresses caused by ionic size mismatch.

SEM study and morphological characterization

SEM images of the $Zn_xCo_{1-x}Fe_2O_4$ (x = 0.0, 0.2, 0.5, 0.6, and 0.7) nanoparticles are presented in Fig. 3a–e, revealing that most particles exhibit a spherical shape and are evenly distributed. Particle size distribution histograms were generated by analyzing the diameters of a minimum of 180 particles in each SEM picture

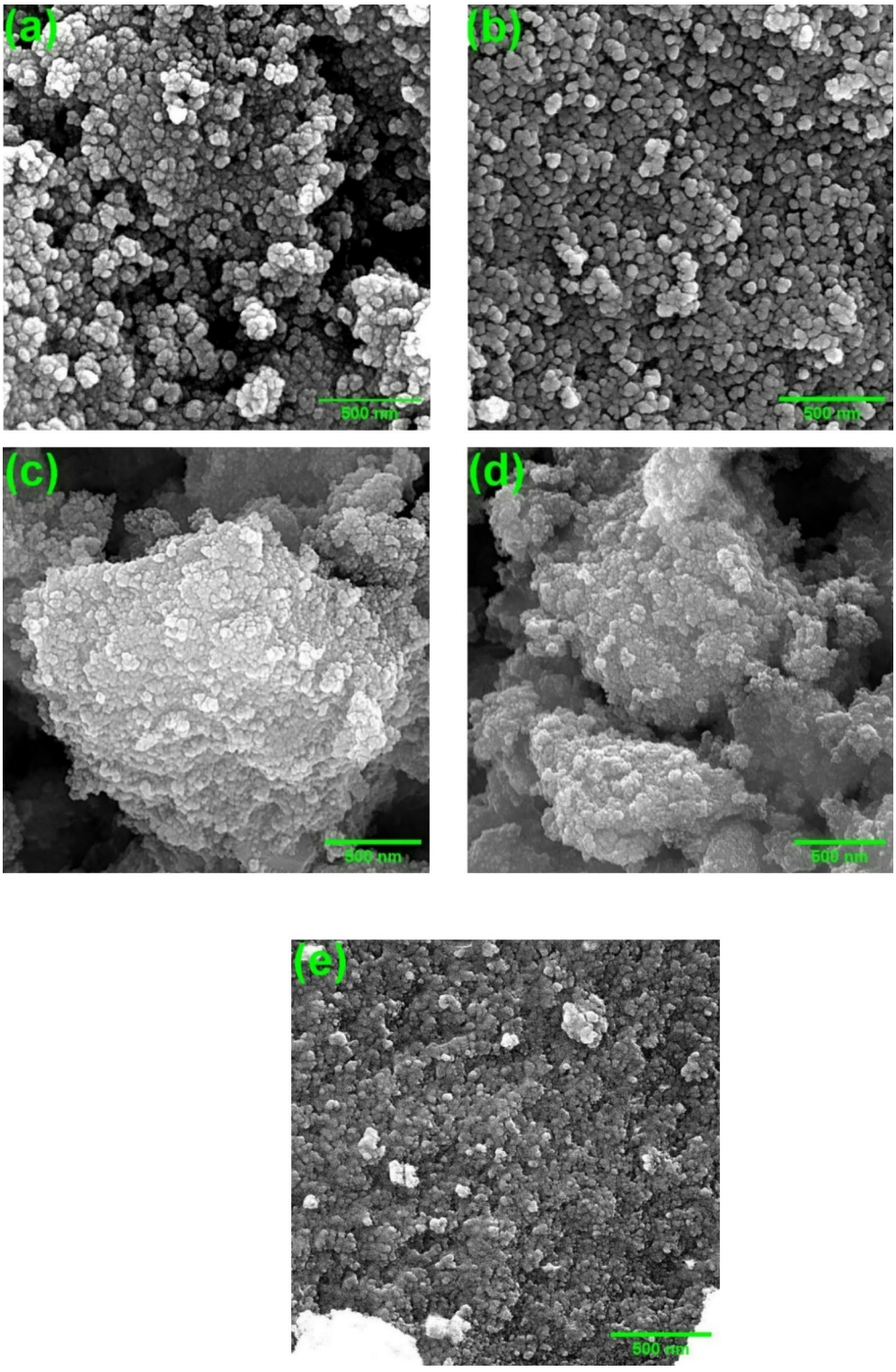

Fig. 3. SEM images of (**a**) $CoFe_2O_4$, (**b**) $Zn_{0.2}Co_{0.8}Fe_2O_4$, (**c**) $Zn_{0.5}Co_{0.5}Fe_2O_4$, (**d**) $Zn_{0.6}Co_{0.4}Fe_2O_4$, and (**e**) $Zn_{0.7}Co_{0.3}Fe_2O_4$ nanoparticles.

utilizing ImageJ software, with the results shown in Fig. 4a–e. For all samples, the particle sizes range between 15 and 60 nm. The mean particle size for each sample was determined by fitting the size distribution histograms to a log-normal distribution function, described by the Eq. (2)[4,67]:

$$f(d) = \left(\frac{1}{\sqrt{2\pi}\,\sigma_D}\right) exp\left[\frac{\left(Ln\left(\frac{d}{D}\right)\right)^2}{2\sigma_D{}^2}\right] \tag{12}$$

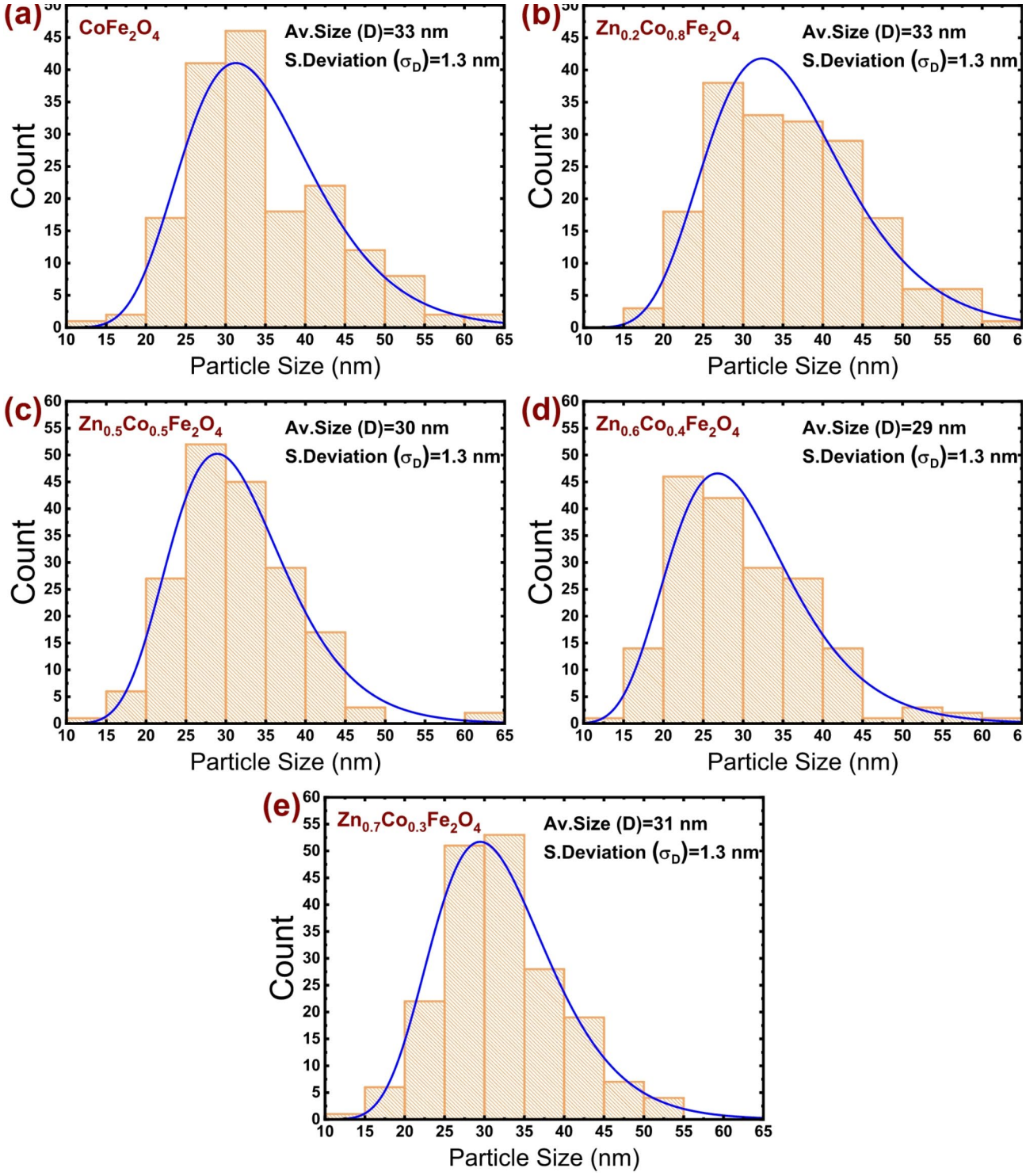

Fig. 4. The size distribution histogram and the log-normal fit for (**a**) $CoFe_2O_4$, (**b**) $Zn_{0.2}Co_{0.8}Fe_2O_4$, (**c**) $Zn_{0.5}Co_{0.5}Fe_2O_4$, (**d**) $Zn_{0.6}Co_{0.4}Fe_2O_4$, and (**e**) $Zn_{0.7}Co_{0.3}Fe_2O_4$ nanoparticles.

where D represents the mean particle size, and σ_D shows the standard deviation. The fit of the log-normal function to the size distribution histograms for each sample is represented by a solid blue line in Fig. 4a–e. The calculated mean particle size and standard deviation for each sample are displayed in the inset of Fig. 4a–e. It can be seen that the average particle size in pure cobalt ferrite (x = 0.0) is 33 nm. With increasing Zn content, the average particle size gradually decreases to 29 nm in the x = 0.6 sample, before increasing to 31 nm in the x = 0.7 sample.

Magnetic properties

Figure 5a represents the magnetic hysteresis curves for $Zn_xCo_{1-x}Fe_2O_4$ (x = 0.0, 0.2, 0.5, 0.6, and 0.7) nanoparticles at room temperature. A magnified view of the loops, around H = 0, is presented in the inset of Fig. 5a. It has been observed that the $CoFe_2O_4$ and $Zn_{0.2}Co_{0.8}Fe_2O_4$ samples show open loops while the other samples have closed loops. Arrott plots were used to determine the ferrimagnetic and superparamagnetic behavior of the samples. The Arrott plot represents the variation of H/M as a function of $M^{[2}$ [24,63,68]. The Arrott plots for all nanoparticles are presented in Fig. 5b. The plots of the $CoFe_2O_4$ and $Zn_{0.2}Co_{0.8}Fe_2O_4$ samples show a clear positive intercept on the M^2 axis at H = 0, indicating spontaneous magnetization, corresponding to the ferrimagnetic phase. In contrast, $Zn_{0.5}Co_{0.5}Fe_2O_4$, $Zn_{0.6}Co_{0.4}Fe_2O_4$, and $Zn_{0.7}Co_{0.3}Fe_2O_4$ samples do not show a clear positive intercept on the M^2 axis at H = 0 Oe, suggesting the absence of spontaneous magnetization, consistent with the superparamagnetic phase. Additionally, the coercivities (H_C) extracted from the hysteresis curves for various nanoparticles are presented in Table 7. The coercivities obtained for $CoFe_2O_4$ and $Zn_{0.2}Co_{0.8}Fe_2O_4$ are 524 Oe and 359 Oe, respectively, while the other samples show zero coercivity. When the size of magnetic nanoparticles decreases below a critical threshold, the thermal energy (K_BT) surpasses the energy barrier, influencing magnetic anisotropy. As a result, thermal fluctuations can reorient the magnetic moments, reducing hysteresis and ultimately eliminating coercivity, leading to superparamagnetism[69]. Based on coercivity values, magnetic materials are classified as hard (H_C > 800 Oe), semi-hard (511 Oe < H_C < 800 Oe), and soft (H_C < 511 Oe) magnetic materials[70]. Therefore, the $CoFe_2O_4$ sample is classified as semi-hard, while $Zn_{0.2}Co_{0.8}Fe_2O_4$ is a soft magnetic material. The $Zn_{0.5}Co_{0.5}Fe_2O_4$, $Zn_{0.6}Co_{0.4}Fe_2O_4$, and $Zn_{0.5}Co_{0.5}Fe_2O_4$ samples, based on their magnetic hysteresis data, can be classified as superparamagnetic.

As shown in Fig. 5(a), the samples do not achieve saturation even at the maximum applied magnetic field of 14 kOe. Therefore, the approach to saturation relation (ASR) has been utilized to determine the samples' saturation magnetization (M_s)[71]. The ASR describes how magnetization (M) depends on the applied magnetic field (H), particularly when the H is much larger than the coercivity H_c. This equation is typically employed to explain magnetization behavior in high magnetic field regions, where the magnetic domain rotation becomes considerable. The relationship is expressed as[72,73]:

$$M = M_S\left(1 - \frac{a}{H} - \frac{b}{H^2}\right) + \chi_P H \tag{13}$$

where a represents the inhomogeneity parameter, b denotes the anisotropy factor and χ_P reflects the high field susceptibility. The $\frac{a}{H}$ term is linked to structural defects and chemical inhomogeneities, originating from non-magnetic sources. The $\frac{b}{H^2}$ term is associated with magnetocrystalline anisotropy and describes the magnetization rotation against the magnetocrystalline anisotropy energy. The $\chi_P H$ term, often referred to as paramagnetic-like, accounts for the field-induced increase in magnetization within magnetic domains[70,72]. The magnetization near the saturation can be expressed as $M = M_S\left(1 - \frac{b}{H^2}\right)$. Therefore, in high magnetic field region, the M versus $\frac{1}{H^2}$ plot exhibits linear behavior, with the intercept corresponding to saturation magnetization[72]. The M versus $\frac{1}{H^2}$ plot and its linear fitting in the H ≥ 9000 Oe region for various nanoparticles are demonstrated in Fig. 6a. The saturation magnetization of the various nanoparticles was determined from the y-intercept of the extrapolated lines in Fig. 6a. As shown in Table 7, the M_s quantity enhances from 60 emu/g in the undoped sample to 68 emu/g in the sample with x = 0.2, then decreases with further Zn doping, reaching 31 emu/g for x = 0.7.

By determining the M_s values, the squareness ratio (M_r/M_s) can be calculated, indicating the material's magnetic domain state. This ratio helps differentiate between single-domain, multi-domain, and pseudo-single-domain states. A material is classified as multi-domain when M_r/M_s is less than 0.1, where changes in magnetization occur through domain wall movement in relatively low magnetic fields. In contrast, magnetization changes primarily through the rotation of domain for single-domain materials (M_r/M_s > 0.5). The material is considered pseudo-single-domain if M_r/M_s falls between 0.1 and 0.5 [72,74,75]. Based on the obtained M_r/M_s values (Table 7), the $CoFe_2O_4$ and $Zn_{0.2}Co_{0.8}Fe_2O_4$ samples exhibit pseudo-single-domain structures, while the remaining three samples show superparamagnetic properties with M_r = 0. The average magnetic domain size can be estimated by the following relation[24,76]

$$D_s = \left[\frac{18k_BT}{\pi\,\rho\,M_s^2}\left(\frac{dM}{dH}\right)_{H=0}\right]^{\frac{1}{3}} \tag{14}$$

where k_B shows the Boltzmann constant, T denotes the Temperature, ρ represents the sample density, M_s is the saturation magnetization, and $\left(\frac{dM}{dH}\right)_{H=0}$ denotes the M-H curve slope at H = 0 Oe. Table 7 records the estimated domain size for different samples. As observed, the domain size grows as the Zn doping level increases up to 0.6 but decreases in the x = 0.7 sample.

The effective anisotropy influences the magnetic characteristics of spinel ferrites, and thus the shape of their magnetic hysteresis loops[77,78]. To estimate the anisotropy field and effective anisotropy constant, the M–H plots

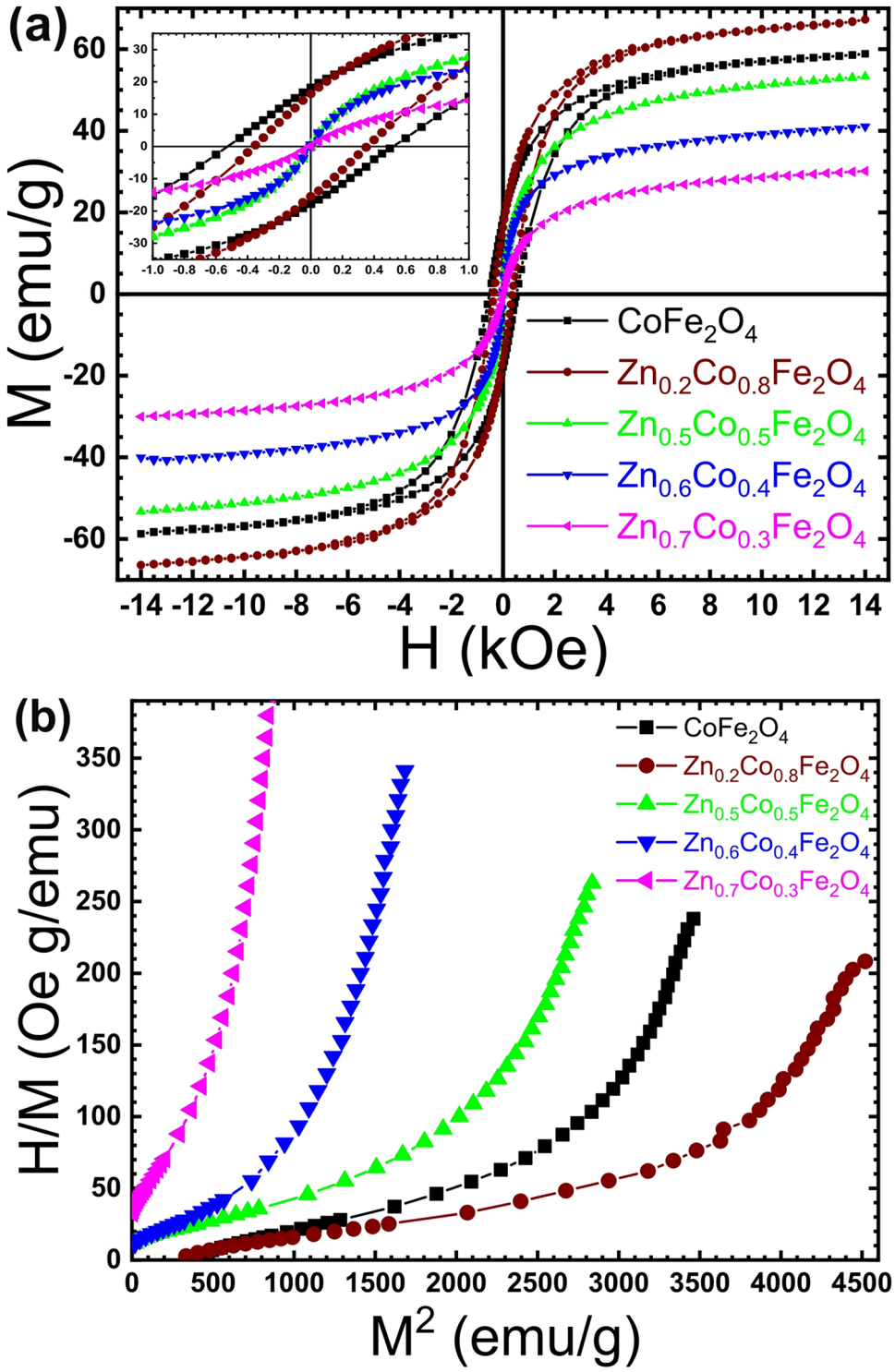

Fig. 5. (a) Room temperature magnetic hysteresis loops (magnified view of the loops, around H = 0 Oe, is presented in the inset) and (b) Arrott plots for different samples.

of the samples were fitted by the empirical formula from LAS theory (Eq. 14). The fitted M-H plots for the different nanoparticles, within the field range of 1000 Oe < H < 14,000 Oe, are presented in Fig. 6b. The solid red lines indicate the fit using LAS theory. The extracted values for a, b, and χ_P parameters are recorded in Table 8. In the overall comparison, it is noticeable that the a and b values decrease in the $Zn_{0.2}Co_{0.8}Fe_2O_4$ sample compared to the undoped sample, but increase with higher doping levels. The higher inhomogeneity parameter a is linked to structural defects, chemical inhomogeneities, and inclusions of non-magnetic ions.

Sample	H_C (Oe)	M_r (emu/g)	M_s (emu/g)	M_r/M_s	D_s (nm)
$CoFe_2O_4$	524	18	60	0.30	7.2
$Zn_{0.2}Co_{0.8}Fe_2O_4$	359	16	68	0.23	7.3
$Zn_{0.5}Co_{0.5}Fe_2O_4$	0	0	55	0.00	10.3
$Zn_{0.6}Co_{0.4}Fe_2O_4$	0	0	42	0.00	12.5
$Zn_{0.7}Co_{0.3}Fe_2O_4$	0	0	31	0.00	10.9

Table 7. Coercivity (H_C), remanent magnetization (M_r), saturation magnetization (Ms), squareness ratio (M_r/M_s), and estimated magnetic domain size (Ds) for various samples.

The parameter b is also related to the anisotropies of the sample and can be determined utilizing the following relation[72]

$$b = \frac{{H_A}^2}{15} = \frac{\left(4K_{eff}^2\right)}{15M_s^2} \tag{15}$$

where H_A represents the anisotropy field and K_{eff} is the effective magneto crystalline anisotropy constant. The values of H_A and K_{eff} were determined using this equation and the estimated b values. The results are summarized in Table 8. The H_A value decreases from 2243 Oe in the undoped sample to 2032 Oe in the sample with x = 0.2, then increases with higher Zn doping, reaching 2743 Oe in the sample with x = 0.7. Similarly, the K_{eff} value rises from 67.3×10^3 emu/cm^3 in the undoped sample to 69.4×10^3 emu/cm^3 for x = 0.2, before declining with further Zn doping, reaching 42.7×10^3 emu/cm^3 for x = 0.7. The overall variation in the anisotropy field (H_A) and effective magneto crystalline anisotropy constant (K_{eff}) is depicted in Fig. 7.

The magnetic moment per formula unit, expressed in Bohr magnetons, is calculated utilizing the equation below[79,80]:

$$\eta_B^{exp} = \frac{M_S \times M_W}{5585} \tag{16}$$

Here, M_W demonstrates the sample molecular weight. The estimated η_B^{exp} value for various nanoparticles are shown in Table 9. Based on the Neel model for ferrimagnetic materials, the magnetic moment per formula unit, in Bohr magnetons, is given by the expression[79,80]:

$$\eta_B^{theo} = M_B - M_A \tag{17}$$

where M_B and M_A represent the magnetic moments of the octahedral (B) and tetrahedral (A) sublattices, respectively, in Bohr magnetons. The η_B^{theo} value for various nanoparticles was calculated utilizing the determined cation distributions across the octahedral and tetrahedral sites (Table 5) and the ionic magnetic moments of Co^{2+}, Zn^{2+}, and Fe^{3+}, which are 1.7 μ_B, 0.0 μ_B, and 5.9 μ_B, respectively[31]. The calculated quantities for M_B, M_A, and η_B^{theo} are presented in Table 9. As shown, the theoretically calculated magnetic moments per formula unit (η_B^{theo}) are greater than those obtained from magnetization measurements (η_B^{exp}). This discrepancy can be explained by spin disorder in the surface regions of the nanoparticles. In fact, surface magnetic order is disrupted by various internal and external factors, such as surface defects, thermal fluctuations, mechanical stress, chemical reactions, particle aggregation, and adsorption-desorption processes[31].

Magnetic hyperthermia properties

To assess the potential of the studied samples for hyperthermia applications, we recorded the inductive heating rate of all prepared samples. Each sample was dissolved in distilled water at a concentration of 1.5 mg/ml and exposed to an alternating magnetic field with amplitudes of 65, 95, and 125 Oe at 250 and 350 kHz frequencies. The temperature vs. time curves for the samples, heated under different magnetic field amplitudes at these frequencies, are plotted in Fig. 8a–e and Fig. 9a–e. The data shows that when the prepared samples are heated, their temperature quickly surges in the first few seconds, after which the rate of increase slows down, eventually approaching stabilization without reaching a clear plateau. Notably, as the magnetic field amplitude increases, the temperature rises accordingly. The conversion of magnetic energy into thermal energy using magnetic nanoparticles exposed to an alternating magnetic field is quantified by the specific loss power (SLP). SLP represents the power produced per unit mass of the magnetic particles[27]. According to linear response theory, it depends on both the properties of the material or sample (such as liquid viscosity, volume, particle concentration, nanoparticle shape, particle size, magnetization relaxation times, magnetic anisotropy, magnetic susceptibility, and saturation magnetization) as well as the experimental conditions (including the amplitude, frequency, and waveform of the alternating magnetic field). The SLP value is determined utilizing the following formula[27,81,82]

$$SLP = \frac{\sum_i m_i c_i}{m_{NPs}} \left(\frac{dT}{dt}\right) \tag{18}$$

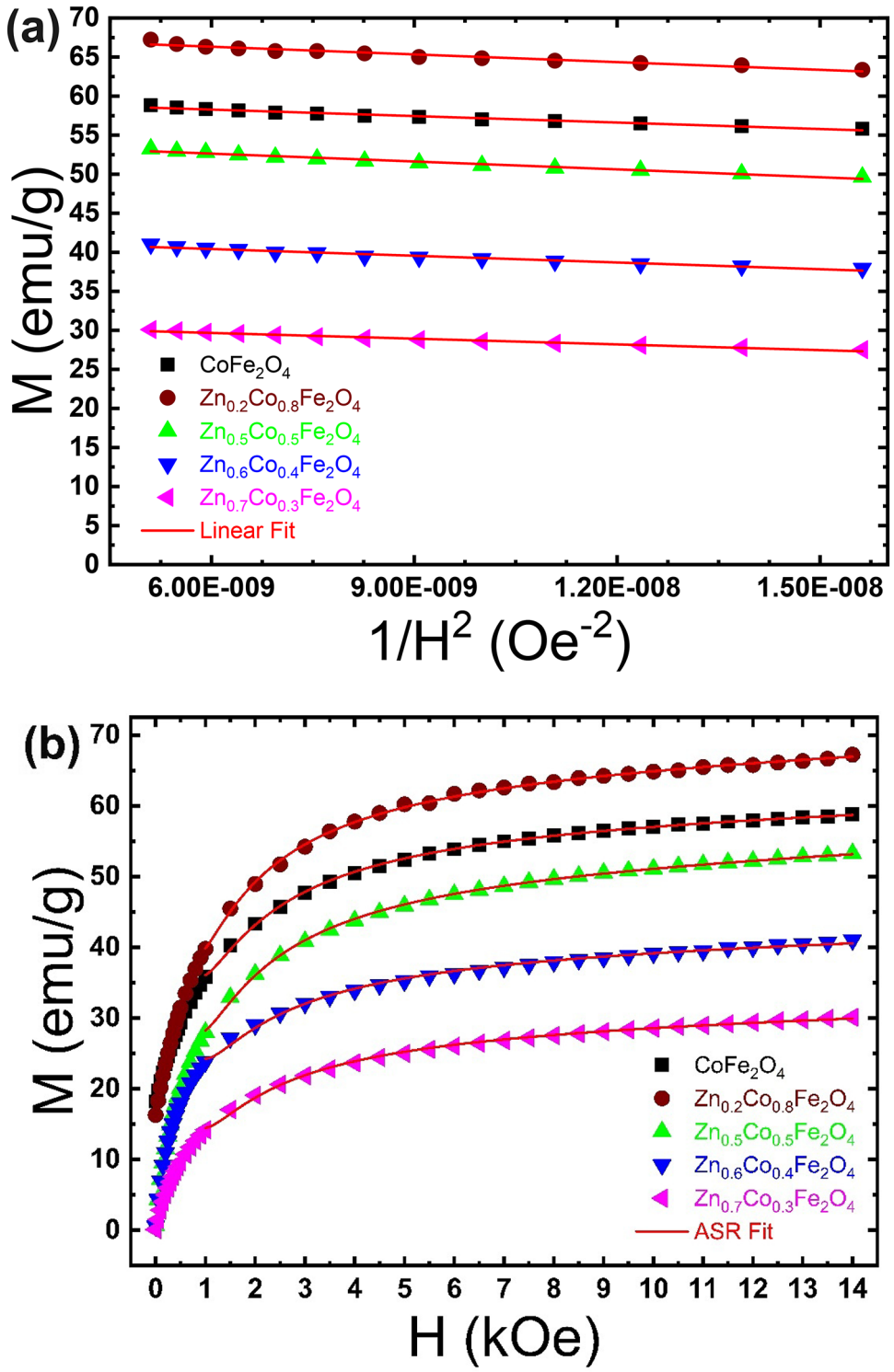

Fig. 6. (**a**) Linear fitting of the M versus $1/H^2$ curve, and (**b**) application of the approach to saturation relation (ASR) to fit the experimental M versus H curves for different samples.

The index *i* refers to the components of the magnetic fluid, specifically magnetic nanoparticles, deionized water, and the thermometer glass. The m_i represents the mass and the c_i shows the specific heat capacity (c_{Water} = 4.18 $Jg^{-1}K^{-1}$, $c_{NPs} = 0.80^{-1}\ K^{-1}$, and $c_{glass} = 0.90^{-1}\ K^{-1}$)[17,81]. The m_{NPs} is the mass of magnetic nanoparticles and the term $\frac{dT}{dt}$ represents the initial slope of the temperature versus the time curve. The SLP values of the samples under investigation have been determined utilizing the initial slope method and the Box-Lucas equation, based on the frequency and amplitude of the applied alternating magnetic field[17]. The initial slope method assumes that heat loss to the surroundings is minimal during the early stages of the heating process, essentially considering

Sample	a (Oe)	b (Oe^2)	χ_p (emu/Oe)	H_A (Oe)	K_{eff} (erg/cm^3)
$CoFe_2O_4$	0.74×10^3	0.34×10^6	1.30×10^{-4}	2246	67.3×10^3
$Zn_{0.2}Co_{0.8}Fe_2O_4$	0.68×10^3	0.27×10^6	2.08×10^{-4}	2032	69.4×10^3
$Zn_{0.5}Co_{0.5}Fe_2O_4$	0.85×10^3	0.38×10^6	$2.18\times10-4$	2389	65.3×10^3
$Zn_{0.6}Co_{0.4}Fe_2O_4$	0.83×10^3	0.41×10^6	$1.34\times10-4$	2493	52.5×10^3
$Zn_{0.7}Co_{0.3}Fe_2O_4$	1.02×10^3	0.50×10^6	$1.39\times10-4$	2743	42.7×10^3

Table 8. Anisotropy factors (a and b), high-field susceptibility (χ_p), anisotropy field (H_A), and magnetocrystalline anisotropy (K_{eff}) determined from the fitting of M-H data for the various samples.

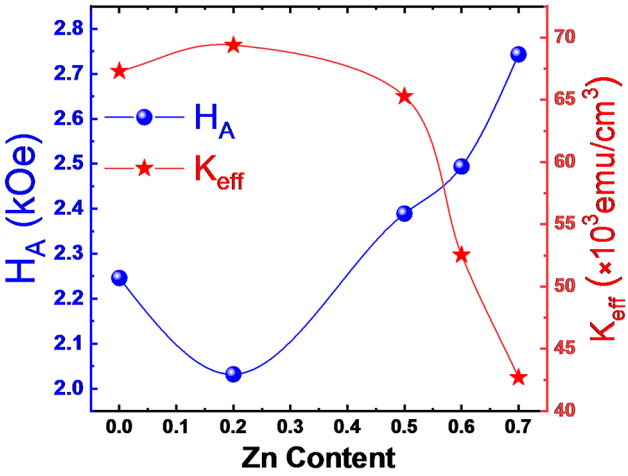

Fig. 7. Variation of the anisotropy field (H_A) and effective magnetocrystalline anisotropy constant (K_{eff}) with Zn content.

Sample	η_B^{exp} (μ_B)	M_B (μ_B)	M_A (μ_B)	$\eta_B^{theo} = M_B - M_A$ (μ_B)
$CoFe_2O_4$	2.51	8.692	4.808	3.884
$Zn_{0.2}Co_{0.8}Fe_2O_4$	2.88	8.437	4.723	3.714
$Zn_{0.5}Co_{0.5}Fe_2O_4$	2.33	8.038	4.612	3.426
$Zn_{0.6}Co_{0.4}Fe_2O_4$	1.80	7.784	4.696	3.088
$Zn_{0.7}Co_{0.3}Fe_2O_4$	1.33	7.631	4.679	2.952

Table 9. Experimental and theoretical values of the magnetic moment per formula unit (η_B) along with the magnetic moments of the octahedral (M_B) and tetrahedral (M_A) sublattices.

adiabatic conditions over a short time interval. This time range is deemed adiabatic as long as the temperature versus time graph remains linear. In this method, the initial slope $\frac{dT}{dt}$ is estimated using the slope of the tangent line at the zero point on the temperature-time graph[26]. The dashed green lines in Figs. 8 and 9 represent the linear fit of the temperature-time curves within the adiabatic region. Figure 10a presents the estimated SLP values for various samples calculated using the initial slope method at magnetic field amplitudes of 65, 95, and 125 Oe, and frequencies of 250 kHz and 350 kHz. As shown, the SLP values for the samples increase with rising magnetic field amplitude and frequency. Additionally, the SLP value increases with Zn doping concentration up to x = 0.6, after which it declines at x = 0.7. These results indicate that the SLP value reaches its maximum at x = 0.6.

Alternatively, to determine the SLP value under non-adiabatic experimental conditions, the initial slope $\frac{dT}{dt}$ can be derived utilizing the Box–Lucas relation, expressed as[17,24,82]

$$\Delta T = A(1 - e^{-Bt}) \tag{19}$$

.

In this equation, the product of the A and B parameters provides the initial slope of the temperature-time curve. Using this approach, the measured data were fitted to Eq. 19, and the initial slope was calculated from the estimated A and B values. The red solid lines in Fig. 8a–e and 9a–e illustrate the fit using the Box-Lucas function.

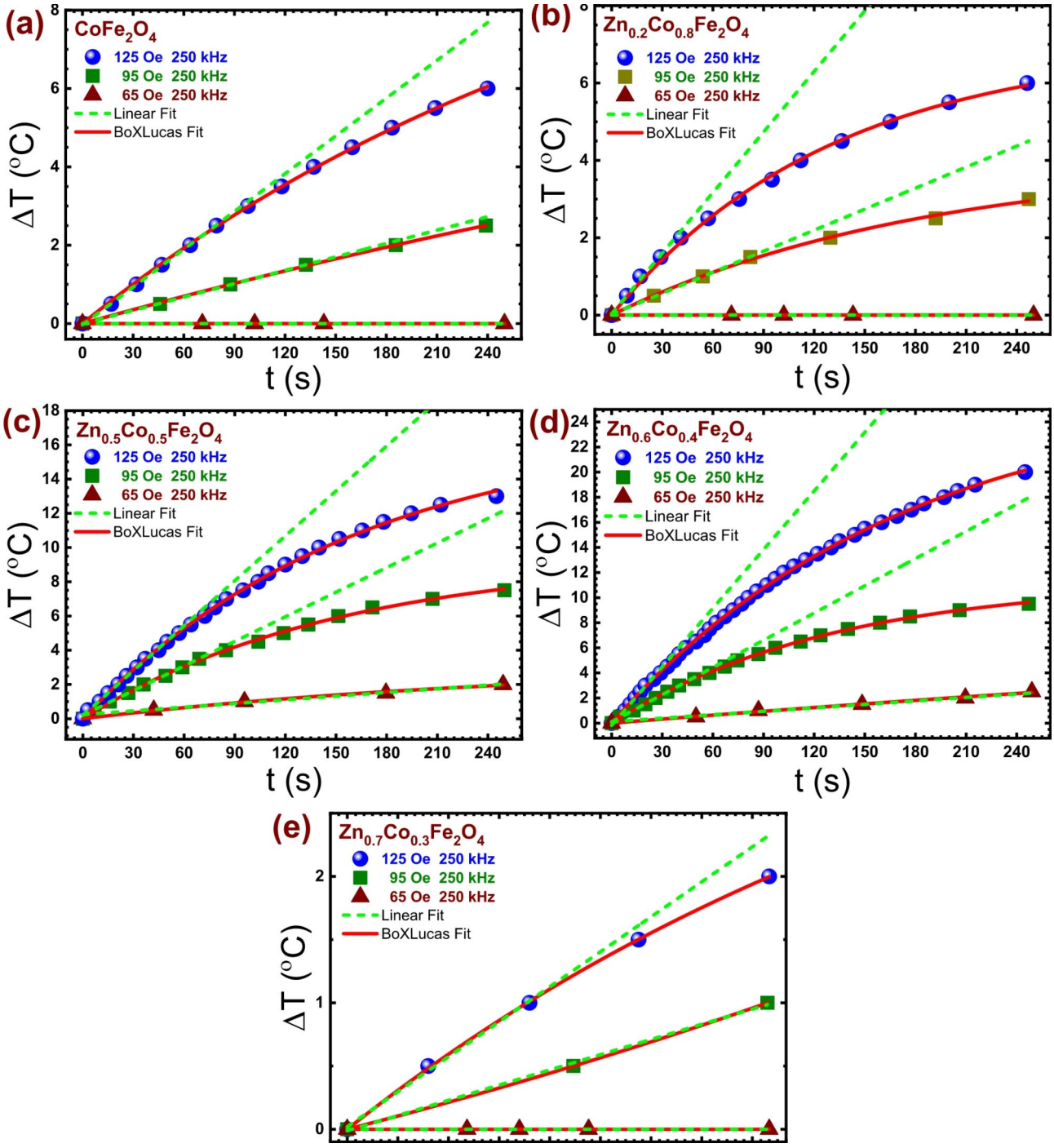

Fig. 8. Magnetic hyperthermia response: Temperature-time profiles of nanoparticles on a water suspension exposed to an alternating magnetic field at a frequency of 250 kHz and amplitudes of 65, 95, and 125 Oe for (**a**) $CoFe_2O_4$, (**b**) $Zn_{0.2}Co_{0.8}Fe_2O_4$, (**c**) $Zn_{0.5}Co_{0.5}Fe_2O_4$, (**d**) $Zn_{0.6}Co_{0.4}Fe_2O_4$, and (**e**) $Zn_{0.7}Co_{0.3}Fe_2O_4$. Red solid curves represent fits using the Box-Lucas equation, while green dashed lines correspond to fits based on linear response theory.

The SLP values estimated for various samples at different magnetic field amplitudes and frequencies, using the Box-Lucas method, are shown in Fig. 10b. These values exhibit a similar trend to those obtained through the initial slope method, but the Box-Lucas values are consistently higher. This systematic discrepancy can primarily be attributed to the initial slope method's omission of heat loss, which the Box-Lucas model accounts for. Unlike the initial slope method, which focuses on the early temperature rise, the Box-Lucas model considers the temperature profile over a longer time scale, capturing the impact of sustained heating[26]. At 350 kHz and a magnetic field amplitude of 125 Oe, the SLP values obtained using the Box–Lucas model for the undoped nanoparticles (x = 0.0) and the nanoparticles with x = 0.2 are 21.03 W/g and 22.72 W/g, respectively. The SLP

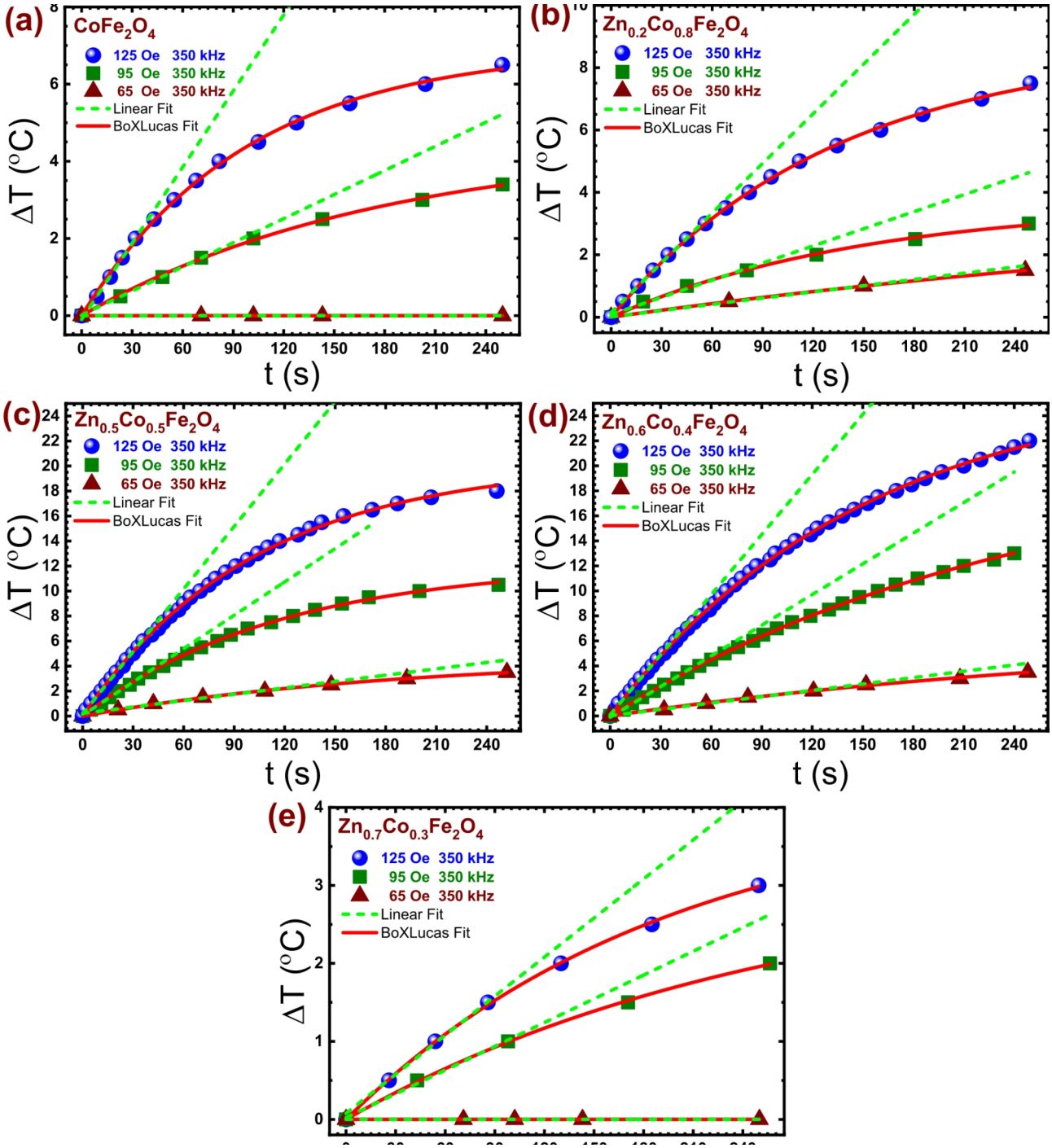

Fig. 9. Magnetic hyperthermia response: Temperature-time profiles of nanoparticles on a water suspension exposed to an alternating magnetic field at a frequency of 350 kHz and amplitudes of 65, 95, and 125 Oe for (**a**) $CoFe_2O_4$, (**b**) $Zn_{0.2}Co_{0.8}Fe_2O_4$, (**c**) $Zn_{0.5}Co_{0.5}Fe_2O_4$, (**d**) $Zn_{0.6}Co_{0.4}Fe_2O_4$, and (**e**) $Zn_{0.7}Co_{0.3}Fe_2O_4$. Red solid curves represent fits using the Box-Lucas equation, while green dashed lines correspond to fits based on linear response theory.

values increase significantly for nanoparticles with x = 0.5 and x = 0.6, reaching 55.60 W/g and 59.86 W/g. However, for the x = 0.7 sample, the SLP decreases to 6.04 W/g. Similarly, at 250 kHz and 125 Oe, the SLP for the x = 0.0 and x = 0.2 samples are 10.41 W/g and 15.28 W/g, respectively, with a rise to 30.08 W/g and 48.71 W/g for the x = 0.5 and x = 0.6 nanoparticles, followed by a drop to 3.04 W/g for the x = 0.7 nanoparticles. These results indicate that the $Zn_{0.6}Co_{0.4}Fe_2O_4$ sample is the most suitable for magnetic hyperthermia applications. Additionally, the maximum product of the applied magnetic field amplitude (125 Oe) and frequency (350 kHz) in this study is 43.8×10^6 Oe/s, which is well below the clinical hyperthermia threshold limit of 63×10^6 Oe/s.

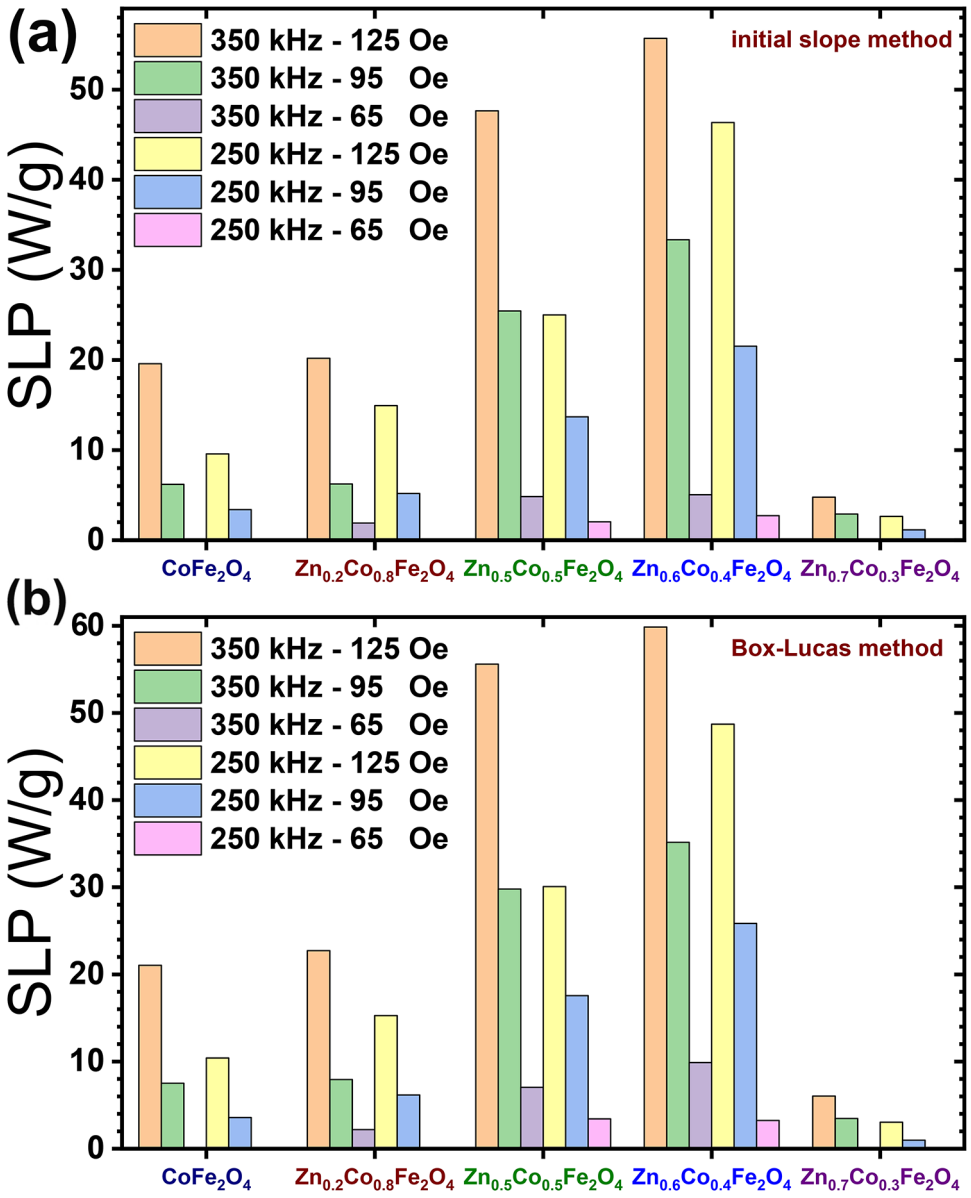

Fig. 10. Specific Loss Power (SLP) quantities for different samples calculated at different alternating magnetic field amplitudes and frequencies using (**a**) the initial slope method and (**b**) the Box–Lucas method.

As the conditions for linear response theory were met in all the experiments conducted in this research, the SLP values are expected to change in proportion to the square of the magnetic field amplitude $(H_0^2)^2$. Figure 11a and b display the SLP values as a function of H_0^2 for various samples at 250 kHz and 350 kHz, respectively. The plots reveal a linear trend across all samples, confirming the quadratic subordination of SLP on the magnetic field amplitude, as predicted by the linear response theory.

The SLP depends on the frequency of the applied alternating magnetic field. To facilitate the comparison of values across different applied fields and frequencies, the Intrinsic Power Loss (IPL) coefficient, measured in nH m^2/kg, has been introduced[83,84]

$$ILP = \frac{SLP}{H_0^2 f} \tag{20}$$

where H_0 represents the magnetic field amplitude, and f denotes the frequency. It is crucial to recognize that the ILP has its limitations and should not be regarded as the definitive parameter for assessing hyperthermia efficiency. As previously mentioned, the SLP value is obtained indirectly and is influenced by the chosen method. Moreover, the relationship $SLP \sim f.H_0^2$ holds only within a narrow range of frequencies and field strengths, or for monodisperse nanoparticle systems with high effective anisotropy[17,85]. Despite this, both SLP and ILP are indicators of the nanoparticles' heating efficiency, with higher values implying that less magnetic material is

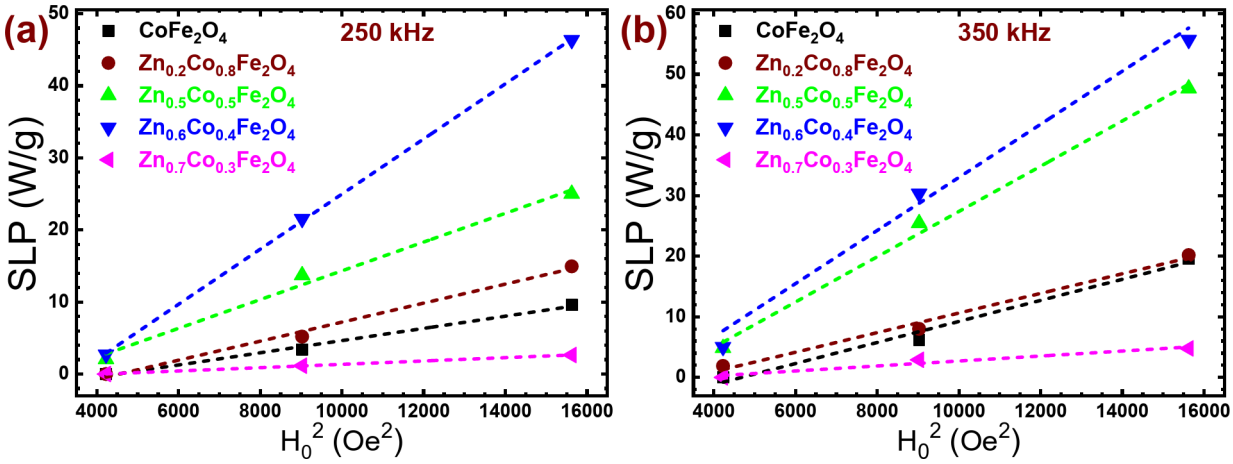

Fig. 11. Specific Loss Power (SLP) versus the square of the alternating magnetic field amplitude (H_0^2) for Zn-substituted $CoFe_2O_4$ nanoparticles at frequencies of (a) 250 kHz and (b) 350 kHz. Dashed lines represent linear fits, highlighting the dependence of SLP on H_0^2.

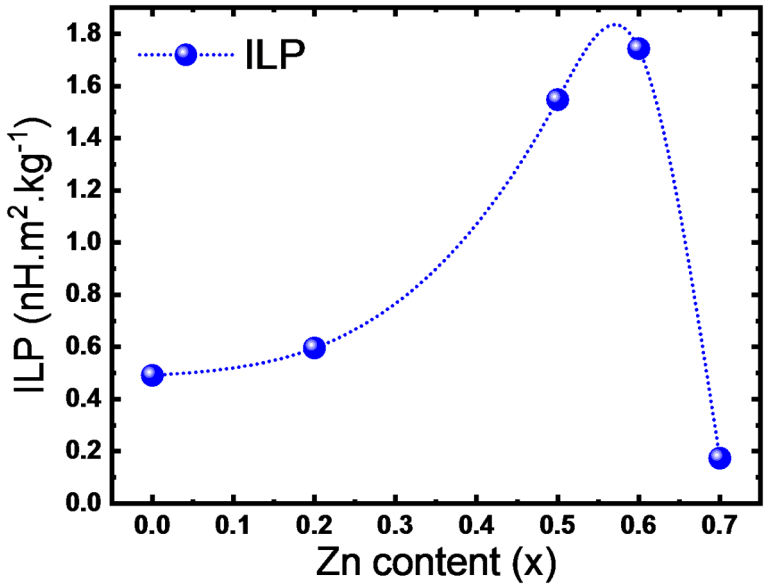

Fig. 12. Variation of the mean Intrinsic Loss Power (ILP) values with Zn content in Zn-substituted $CoFe_2O_4$ nanoparticles.

required for hyperthermia applications[17]. Figure 12 displays the estimated mean ILP values plotted as a function of Zn content. The mean ILP value for x = 0.0 is 0.49 nH m^2/kg. This value increases with the increase of Zn concentration and reaches 0.59 nH m^2/kg and 1.55 nH m^2/kg for x = 0.2 and x = 0.5, respectively, and reaches its maximum value of 1.74 nH m^2/kg for x = 0.6. For x = 0.7, the ILP value decreases sharply and reaches 0.17 nH m^2/kg.

Heat generation in a liquid medium containing magnetic nanoparticles exposed to a radio frequency alternating magnetic field is generally attributed to three possible mechanisms: eddy current losses, magnetic hysteresis losses, and relaxation losses[22]. Spinel ferrites, such as cobalt ferrite ($CoFe_2O_4$) and zinc-substituted cobalt ferrite ($Zn_xCo_{1-x}Fe_2O_4$), exhibit low electrical conductivity, behaving similarly to semiconductors. As a result, when these samples interact with an alternating magnetic field, the induced eddy currents are minimal, and the heat generated by this mechanism is negligible.

Magnetic hysteresis loss is proportional to the area enclosed by the magnetic hysteresis loop. The x = 0.5, 0.6, and 0.7 samples exhibit closed hysteresis loops, indicating superparamagnetic behavior. Thus, the heat produced from hysteresis losses is insignificant in these samples and only relevant for those with x = 0.0 and x = 0.2. Therefore, for the x = 0.5, 0.6, and 0.7 samples, the primary source of heat generation is the relaxation loss mechanism, which includes Brownian and Néel relaxation processes.

Sample	τ_B (s)	τ_N (s)	τ_R (s)
$CoFe_2O_4$	1.44714×10^{-5}	18975.78599	1.44714×10^{-5}
$Zn_{0.2}Co_{0.8}Fe_2O_4$	1.44714×10^{-5}	48837.43253	1.44714×10^{-5}
$Zn_{0.5}Co_{0.5}Fe_2O_4$	1.10600×10^{-5}	4.75635	1.10600×10^{-5}
$Zn_{0.6}Co_{0.4}Fe_2O_4$	1.00552×10^{-5}	0.01086	1.00459×10^{-5}
$Zn_{0.7}Co_{0.3}Fe_2O_4$	1.21296×10^{-5}	0.00964	1.21144×10^{-5}

Table 10. Brownian (τ_B), néel (τ_N), and effective (τ_R) relaxation times for various samples.

In Brownian relaxation, the magnetic moment is locked to the crystallographic easy axis, causing the entire nanoparticle to rotate when subjected to an external magnetic field. This rotation leads to energy dissipation as heat due to viscous friction between the particles and the surrounding fluid. The heat produced through this mechanical friction is characterized by the Brownian relaxation time, given by[86–88]:

$$\tau_B = \frac{3\eta V_h}{K_B T} \tag{21}$$

where η is the fluid's viscosity, V_h is the hydrodynamic volume of the nanoparticle, k_B is the Boltzmann constant, and T is the temperature.

In Néel relaxation, the particles remain stationary within the crystal, and their magnetic moments rotate against the magnetic anisotropy energy barrier $E = K_{eff}V$, leading to energy dissipation as heat. The Néel relaxation time is expressed as[86–88]:

$$\tau_N = \tau_0 \exp\left(\frac{K_{eff}V}{K_B T}\right) \tag{22}$$

where τ_0 is the inverse attempt frequency, dependent on intrinsic characteristics like saturation magnetization and magnetic anisotropy, typically ranging from 10^{-13} to 10^{-8} seconds, with a common value of 10^{-9} seconds for spherical spinel ferrites nanoparticles. *V* represents the magnetic volume of the nanoparticle[2,17].

Since both Brownian and Néel relaxation mechanisms often contribute to heat generation simultaneously, the effective relaxation time is expressed as[86–89]:

$$\tau = \frac{\tau_B \tau_N}{(\tau_B + \tau_N)} \tag{23}$$

The Brownian, Néel, and effective relaxation times for the samples were estimated by the aforementioned relations and are summarized in Table 10. It was observed that the Brownian relaxation time remains almost consistent across all samples, whereas the Néel relaxation time is significantly higher for the undoped sample (x = 0.0) and the x = 0.2 sample, but declines sharply for the others. According to linear response theory, a shorter relaxation time correlates with a higher SLP value. Therefore, the enhanced SLP values observed for the nanoparticles with x = 0.5 and x = 0.6 can be attributed to their lower effective relaxation times.

Conclusion

This study provides a comprehensive understanding of the structural, magnetic, and magnetic hyperthermia properties of Zn-substituted cobalt ferrite ($Zn_xCo_{1-x}Fe_2O_4$) nanoparticles, demonstrating how Zn incorporation systematically alters their physical characteristics. The Rietveld refinement of X-ray diffraction patterns confirmed the formation of a pure spinel phase with notable cation redistribution, leading to lattice distortions and modifications in the oxygen positional parameter. The variation in magnetic properties, including the transition from ferrimagnetic to superparamagnetic behavior, the coercivity reduction, and the peak in saturation magnetization at x = 0.2 was attributed to changes in superexchange interactions due to Zn substitution.

In terms of magnetic hyperthermia performance, $Zn_{0.6}Co_{0.4}Fe_2O_4$ exhibited the highest heating efficiency, as reflected in its superior specific loss power (SLP) and intrinsic loss power (ILP) under alternating magnetic fields and frequencies. The quadratic dependence of SLP on the magnetic field amplitude confirmed the validity of the linear response theory, ensuring controlled and efficient heat generation. Importantly, the optimized Zn content led to a balance between thermal efficiency and magnetic softness, making the material highly suitable for hyperthermia applications. A critical aspect of this study is the role of Zn substitution in tuning the magnetic anisotropy and relaxation mechanisms. The dominant contribution of Néel and Brownian relaxation losses over hysteresis heating in the superparamagnetic samples underscores their potential for biomedical applications. Furthermore, the low field and frequency requirements for effective heating place these materials well within clinically accepted safety limits, reinforcing their viability for in vivo applications.

Beyond hyperthermia, these findings suggest that Zn-substituted $CoFe_2O_4$ nanoparticles hold promise for broader applications in biomedicine, including targeted drug delivery and bio-imaging, due to their tunable magnetic response. Future research should focus on surface functionalization and in vivo biocompatibility to facilitate clinical translation. The insights gained from this work contribute to the rational design of high-performance magnetic nanomaterials, advancing their potential for next-generation biomedical applications.

Data availability

The datasets used and/or analyzed during the current study are available from the corresponding author upon reasonable request.

Received: 9 January 2025; Accepted: 14 March 2025
Published online: 24 March 2025

References

1. Bray, F. et al. Global cancer statistics 2018: GLOBOCAN estimates of incidence and mortality worldwide for 36 cancers in 185 countries. *Cancer J. Clin.* **68**, 394–424. https://doi.org/10.3322/caac.21492 (2018).
2. Hadadian, Y., Ramos, A. P. & Pavan, T. Z. Role of zinc substitution in magnetic hyperthermia properties of magnetite nanoparticles: interplay between intrinsic properties and dipolar interactions. *Sci. Rep.* **9**, 18048. https://doi.org/10.1038/s41598-019-54250-7 (2019).
3. Joo, J. in *Advanced Imaging and Bio Techniques for Convergence Science* (eds J. K. Kim, J. K. Kim, & C.-G. Pack), 401–447 (Springer, 2021).
4. Farzin, A., Etesami, S. A., Quint, J., Memic, A. & Tamayol, A. Magnetic nanoparticles in cancer therapy and diagnosis. *Adv. Healthc. Mater.* **9**, 1901058. https://doi.org/10.1002/adhm.201901058 (2020).
5. Cruz, M. M. et al. *Nanostructures for Cancer Therapy* (eds A. Ficai & A. M. Grumezescu), 485–511 (2017).
6. Materón, E. M. et al. Magnetic nanoparticles in biomedical applications: A review. *Appl. Surf. Sci. Adv.* **6**, 100163. https://doi.org/10.1016/j.apsadv.2021.100163 (2021).
7. Kandasamy, G. & Maity, D. Multifunctional theranostic nanoparticles for biomedical cancer treatments - A comprehensive review. *Mater. Sci. Engineering: C.* **127**, 112199. https://doi.org/10.1016/j.msec.2021.112199 (2021).
8. Krishnan, R. Cytotoxicity and heating efficiency of dendrimer functionalized graphene oxide modified nickel ferrite nanoparticles. *Chem. Phys. Lett.* **848**, 141399. https://doi.org/10.1016/j.cplett.2024.141399 (2024).
9. Wells, J. et al. Lissajous scanning magnetic particle imaging as a multifunctional platform for magnetic hyperthermia therapy. *Nanoscale* **12**, 18342–18355. https://doi.org/10.1039/D0NR00604A (2020).
10. Gavilán, H. et al. Magnetic nanoparticles and clusters for magnetic hyperthermia: optimizing their heat performance and developing combinatorial therapies to tackle cancer. *Chem. Soc. Rev.* **50**, 11614–11667. https://doi.org/10.1039/D1CS00427A (2021).
11. Kumar, C. S. S. R. & Mohammad, F. Magnetic nanomaterials for hyperthermia-based therapy and controlled drug delivery. *Adv. Drug Deliv. Rev.* **63**, 789–808. https://doi.org/10.1016/j.addr.2011.03.008 (2011).
12. Tong, S., Zhu, H. & Bao, G. Magnetic iron oxide nanoparticles for disease detection and therapy. *Mater. Today*. **31**, 86–99. https://doi.org/10.1016/j.mattod.2019.06.003 (2019).
13. Manohar, A., Krishnamoorthi, C., Naidu, K. C. B. & Pavithra, C. Dielectric, magnetic hyperthermia, and photocatalytic properties of ZnFe2O4 nanoparticles synthesized by solvothermal reflux method. *Appl. Phys. A*. **125**, 477. https://doi.org/10.1007/s00339-019-2760-0 (2019).
14. Manohar, A., Krishnamoorthi, C., Naidu, K. C. B., Narasaiah, B. P. & Dielectric Magnetic hyperthermia and photocatalytic properties of $Mg_{0.7}Zn_{0.3}Fe_2O_4$ nanocrystals. *IEEE Trans. Magn.* **56**, 1–7. https://doi.org/10.1109/TMAG.2020.3024717 (2020).
15. Kim, J. & Bae, S. Reliable evaluation method of heating power of magnetic nanofluids to directly predict the tumor temperature during hyperthermia. *Sci. Rep.* **11**, 22028. https://doi.org/10.1038/s41598-021-01321-3 (2021).
16. Mohammed, L., Gomaa, H. G., Ragab, D. & Zhu, J. Magnetic nanoparticles for environmental and biomedical applications: A review. *Particuology* **30**, 1–14. https://doi.org/10.1016/j.partic.2016.06.001 (2017).
17. Zeleňáková, A. et al. Cobalt-ferrite nano-cubes for magnetic hyperthermia applications. *J. Alloys Compd.* **989**, 174415. https://doi.org/10.1016/j.jallcom.2024.174415 (2024).
18. Dürr, S. et al. Magnetic nanoparticles for cancer therapy. *Nanatechnol. Reviews.* **2**, 395–409. https://doi.org/10.1515/ntrev-2013-0011 (2013).
19. Pankhurst, Q. A., Thanh, N. T. K., Jones, S. K. & Dobson, J. Progress in applications of magnetic nanoparticles in biomedicine. *J. Phys. D*. **42**, 224001. https://doi.org/10.1088/0022-3727/42/22/224001 (2009).
20. Etemadi, H. & Plieger, P. G. Magnetic fluid hyperthermia based on magnetic nanoparticles: physical characteristics, historical perspective, clinical trials, technological challenges, and recent advances. *Adv. Ther.* **3**, 2000061. https://doi.org/10.1002/adtp.202000061 (2020).
21. Albarqi, H. A. et al. Systemically delivered magnetic hyperthermia for prostate cancer treatment. *Pharmaceutics* **12**, 1020 (2020).
22. Shaterabadi, Z., Nabiyouni, G. & Soleymani, M. Physics responsible for heating efficiency and self-controlled temperature rise of magnetic nanoparticles in magnetic hyperthermia therapy. *Prog. Biophys. Mol. Biol.* **133**, 9–19. https://doi.org/10.1016/j.pbiomolbio.2017.10.001 (2018).
23. Lemine, O. M., Madkhali, N., Hjiri, M., All, N. A. & Aida, M. S. Comparative heating efficiency of hematite (α-Fe2O3) and nickel ferrite nanoparticles for magnetic hyperthermia application. *Ceram. Int.* **46**, 28821–28827. https://doi.org/10.1016/j.ceramint.2020.08.047 (2020).
24. Paswan, S. K. et al. Optimization of structure-property relationships in nickel ferrite nanoparticles annealed at different temperature. *J. Phys. Chem. Solids*. **151**, 109928. https://doi.org/10.1016/j.jpcs.2020.109928 (2021).
25. Ruta, S., Chantrell, R. & Hovorka, O. Unified model of hyperthermia via hysteresis heating in systems of interacting magnetic nanoparticles. *Sci. Rep.* **5**, 9090. https://doi.org/10.1038/srep09090 (2015).
26. Iglesias, C. A. M. et al. Magnetic nanoparticles hyperthermia in a non-adiabatic and radiating process. *Sci. Rep.* **11**, 11867. https://doi.org/10.1038/s41598-021-91334-9 (2021).
27. Branquinho, L. C. et al. Effect of magnetic dipolar interactions on nanoparticle heating efficiency: implications for cancer hyperthermia. *Sci. Rep.* **3**, 2887. https://doi.org/10.1038/srep02887 (2013).
28. Ilg, P. & Kröger, M. Field- and concentration-dependent relaxation of magnetic nanoparticles and optimality conditions for magnetic fluid hyperthermia. *Sci. Rep.* **13**, 16523. https://doi.org/10.1038/s41598-023-43140-8 (2023).
29. Atkinson, W. J., Brezovich, I. A. & Chakraborty, D. P. Usable frequencies in hyperthermia with thermal seeds. *IEEE Trans. Biomed. Eng.* **BME-31**, 70–75. https://doi.org/10.1109/TBME.1984.325372 (1984).
30. Hergt, R., Dutz, S., Müller, R. & Zeisberger, M. Magnetic particle hyperthermia: Nanoparticle magnetism and materials development for cancer therapy. *J. Phys.: Condens. Matter*. **18**. https://doi.org/10.1088/0953-8984/18/38/S26 (2006).
31. Aftabi, A. & Ghasemi, F. Boosting photoelectrochemical performance through appling magnetic field in manganese-doped Cobalt ferrite photoanodes. *Fuel* **371**, 132051. https://doi.org/10.1016/j.fuel.2024.132051 (2024).
32. Sagar, T. V., Rao, T. S. & Naidu, K. C. B. Effect of calcination temperature on optical, magnetic and dielectric properties of Sol-Gel synthesized Ni0.2Mg0.8-xZnxFe2O4 (x = 0.0–0.8). *Ceram. Int.* **46**, 11515–11529. https://doi.org/10.1016/j.ceramint.2020.01.178 (2020).
33. Rigato, F. et al. Strain-induced stabilization of new magnetic spinel structures in epitaxial oxide heterostructures. *Mater. Sci. Engineering: B.* **144**, 43–48. https://doi.org/10.1016/j.mseb.2007.07.102 (2007).

34. Rana, S., Philip, J. & Raj, B. Micelle based synthesis of Cobalt ferrite nanoparticles and its characterization using fourier transform infrared transmission spectrometry and thermogravimetry. *Mater. Chem. Phys.* **124**, 264–269. https://doi.org/10.1016/j.matchemphys.2010.06.029 (2010).
35. Mozaffari, M., Hadadian, Y., Aftabi, A. & Oveisy Moakhar, M. The effect of Cobalt substitution on magnetic hardening of magnetite. *J. Magn. Magn. Mater.* **354**, 119–124. https://doi.org/10.1016/j.jmmm.2013.10.039 (2014).
36. Boda, N. et al. Effect of rare Earth elements on low temperature magnetic properties of Ni and Co-ferrite nanoparticles. *J. Magn. Magn. Mater.* **473**, 228–235. https://doi.org/10.1016/j.jmmm.2018.10.023 (2019).
37. Zheng, Y. F. Oxygen isotope fractionation in magnetites: structural effect and oxygen inheritance. *Chem. Geol.* **121**, 309–316. https://doi.org/10.1016/0009-2541(94)00149-3 (1995).
38. Kumar, L., Kumar, P., Narayan, A. & Kar, M. Rietveld analysis of XRD patterns of different sizes of nanocrystalline Cobalt ferrite. *Int. Nano Lett.* **3**, 8. https://doi.org/10.1186/2228-5326-3-8 (2013).
39. Islam, M. A. et al. Structural characteristics, cation distribution, and elastic properties of Cr3 + substituted stoichiometric and non-stoichiometric Cobalt ferrites. *RSC Adv.* **12**, 8502–8519. https://doi.org/10.1039/D1RA09090A (2022).
40. Ding, L. L. et al. Study of cation distributions in spinel ferrites MxMn1-xFe2O4 (M = Zn, Mg, Al). *AIP Adv.* **6**, 105012. https://doi.org/10.1063/1.4966253 (2016).
41. Patange, S. M. et al. Rietveld structure refinement, cation distribution and magnetic properties of Al3 + substituted NiFe2O4 nanoparticles. *J. Appl. Phys.* **109**, 053909. https://doi.org/10.1063/1.3559266 (2011).
42. Ajroudi, L. et al. Magnetic, electric and thermal properties of Cobalt ferrite nanoparticles. *Mater. Res. Bull.* **59**, 49–58. https://doi.org/10.1016/j.materresbull.2014.06.029 (2014).
43. Lima, A. C. et al. Evaluation of (BH)max and magnetic anisotropy of Cobalt ferrite nanoparticles synthesized in gelatin. *Ceram. Int.* **41**, 11804–11809. https://doi.org/10.1016/j.ceramint.2015.05.148 (2015).
44. Zeng, X. et al. Direct observation of cation distributions of ideal inverse spinel CoFe2O4 nanofibres and correlated magnetic properties. *Nanoscale* **9**, 7493–7500. https://doi.org/10.1039/C7NR02013A (2017).
45. Baričić, M. et al. Chemical engineering of cationic distribution in spinel ferrite nanoparticles: the effect on the magnetic properties. *Phys. Chem. Chem. Phys.* **26**, 6325–6334. https://doi.org/10.1039/D3CP06029B (2024).
46. Manh, D. H., Thanh, T. D., Phan, T. L. & Yang, D. S. Towards hard-magnetic behavior of CoFe2O4 nanoparticles: a detailed study of crystalline and electronic structures, and magnetic properties. *RSC Adv.* **13**, 8163–8172. https://doi.org/10.1039/D3RA00525A (2023).
47. Nguyen, L. H. et al. Effect of Gd substitution on structure, optical and magnetic properties, and heating efficiency of Fe3O4 nanoparticles for magnetic hyperthermia applications. *J. Alloys Compd.* **968**, 172205. https://doi.org/10.1016/j.jallcom.2023.172205 (2023).
48. Sabale, S., Jadhav, V., Mane-Gavade, S. & Yu, X. Y. Superparamagnetic CoFe2O4@Au with high specific absorption rate and intrinsic loss power for magnetic fluid hyperthermia applications. *Acta Metall. Sinica (English Letters)*. **32**, 719–725. https://doi.org/10.1007/s40195-018-0830-5 (2019).
49. Munjal, S., Khare, N., Nehate, C. & Koul, V. Water dispersible CoFe2O4 nanoparticles with improved colloidal stability for biomedical applications. *J. Magn. Magn. Mater.* **404**, 166–169. https://doi.org/10.1016/j.jmmm.2015.12.017 (2016).
50. Sanpo, N. et al. Biocompatibility of transition metal-substituted Cobalt ferrite nanoparticles. *J. Nanopart. Res.* **16**, 2510. https://doi.org/10.1007/s11051-014-2510-3 (2014).
51. Kiani, M. N. et al. Synthesis and characterization of Cobalt-Doped ferrites for biomedical applications. *ACS Omega*. **8**, 3755–3761. https://doi.org/10.1021/acsomega.2c05226 (2023).
52. Sanpo, N., Berndt, C. C., Wen, C. & Wang, J. Transition metal-substituted Cobalt ferrite nanoparticles for biomedical applications. *Acta Biomater.* **9**, 5830–5837. https://doi.org/10.1016/j.actbio.2012.10.037 (2013).
53. Khedri, H. & Gholizadeh, A. Experimental comparison of structural, magnetic and elastic properties of M0.3Cu0.2Zn0.5Fe2O4 (M = Cu, Mn, Fe, Co, Ni, Mg) nanoparticles. *Appl. Phys. A.* **125**, 709. https://doi.org/10.1007/s00339-019-3010-1 (2019).
54. Ballirano, P. Effects of the choice of different ionization level for scattering curves and correction for small preferred orientation in Rietveld refinement: the MgAl2O4 test case. *J. Appl. Crystallogr.* **36**, 1056–1061. https://doi.org/10.1107/S0021889803010410 (2003).
55. Khalaf, K. A. M. et al. Influence of Zn2 + ions on the structural and electrical properties of Mg1 – xZnxFeCrO4 spinels. *J. Alloys Compd.* **657**, 733–747. https://doi.org/10.1016/j.jallcom.2015.10.157 (2016).
56. Pottker, W. E. et al. Influence of order-disorder effects on the magnetic and optical properties of NiFe2O4 nanoparticles. *Ceram. Int.* **44**, 17290–17297. https://doi.org/10.1016/j.ceramint.2018.06.190 (2018).
57. Poudel, T. P. et al. The effect of gadolinium substitution in inverse spinel nickel ferrite: structural, magnetic, and Mössbauer study. *J. Alloys Compd.* **802**, 609–619. https://doi.org/10.1016/j.jallcom.2019.06.201 (2019).
58. Kugimiya, K. & Steinfink, H. Influence of crystal radii and electronegativities on the crystallization of AB2X4 stoichiometries. *Inorg. Chem.* **7**, 1762–1770. https://doi.org/10.1021/ic50067a015 (1968).
59. Vara Prasad, B. B. V. S., Ramesh, K. V. & Srinivas, A. Structural and magnetic properties of nanocrystalline nickel ferrite (NiFe2O4) synthesized in sol-gel and combustion routes. *Solid State Sci.* **86**, 86–97. https://doi.org/10.1016/j.solidstatesciences.2018.10.008 (2018).
60. Prasad, B. B. V. S. V. Cation distribution, structural and electric studies on cadmium substituted nickel–zinc ferrite. *Mod. Phys. Lett. B.* **28**, 1450155. https://doi.org/10.1142/s0217984914501553 (2014).
61. Lakhani, V. K., Pathak, T. K., Vasoya, N. H. & Modi, K. B. Structural parameters and X-ray Debye temperature determination study on copper-ferrite-aluminates. *Solid State Sci.* **13**, 539–547. https://doi.org/10.1016/j.solidstatesciences.2010.12.023 (2011).
62. Monisha, P., Priyadharshini, P., Gomathi, S. S. & Pushpanathan, K. Influence of Mn Dopant on the crystallite size, optical and magnetic behaviour of CoFe2O4 magnetic nanoparticles. *J. Phys. Chem. Solids.* **148**, 109654. https://doi.org/10.1016/j.jpcs.2020.109654 (2021).
63. Somvanshi, A. et al. Tuning of magnetic properties and multiferroic nature: case study of cobalt-doped NdFeO3. *Appl. Phys. A.* **127**, 174. https://doi.org/10.1007/s00339-021-04329-8 (2021).
64. Manh, D. H. et al. Determination of the crystalline size of hexagonal La1 – xSrxMnO3 (x = 0.3) nanoparticles from X-ray diffraction – a comparative study. *RSC Adv.* **13**, 25007–25017. https://doi.org/10.1039/D3RA04018F (2023).
65. Kumar, N. S., Suvarna, R. P. & Naidu, K. C. B. Negative dielectric behavior in tetragonal La0.8Co0.2-xEuxTiO3 (x = 0.01–0.04) nanorods. *Mater. Charact.* **166**, 110425. https://doi.org/10.1016/j.matchar.2020.110425 (2020).
66. Suresh Kumar, N. & Padma Suvarna, R. Chandra Babu Naidu, K. Structural and ferroelectric properties of microwave heated lead Cobalt titanate nanoparticles synthesized by sol–gel technique. *J. Mater. Sci.: Mater. Electron.* **29**, 4738–4742. https://doi.org/10.1007/s10854-017-8429-6 (2018).
67. Jalili, H., Aslibeiki, B., Ghotbi Varzaneh, A. & Chernenko, V. A. The effect of magneto-crystalline anisotropy on the properties of hard and soft magnetic ferrite nanoparticles. *Beilstein J. Nanotechnol.* **10**, 1348–1359. https://doi.org/10.3762/bjnano.10.133 (2019).
68. Rmili, N. et al. Magnetocaloric and induction heating characteristics of La0.71Sr0.29Mn0.95Fe0.05O3 nanoparticles. *J. Solgel Sci. Technol.* https://doi.org/10.1007/s10971-024-06361-5 (2024).
69. D, S. et al. Structural characterization and dielectric studies of superparamagnetic iron oxide nanoparticles. *J. Korean Ceram. Soc.* **55**, 230–238. https://doi.org/10.4191/kcers.2018.55.3.02 (2018).

70. Sahu, P., Sahu, P. K. & Panigrahi, S. Investigation of the structural, electrical, and magnetic behavior of Co3+-Ti4 + doped strontium hexaferrite: validation of measured and theoretical models. *J. Mater. Sci.: Mater. Electron.* **35**, 709. https://doi.org/10.1007/s10854-024-12356-3 (2024).
71. Brown, W. F. Theory of the approach to magnetic saturation. *Phys. Rev.* **58**, 736–743. https://doi.org/10.1103/PhysRev.58.736 (1940).
72. Islam, M. R. et al. Structural, thermodynamic, and magnetic properties of SrFe12O19 hexaferrite modified by co-substitution of Cu and Gd. *RSC Adv.* **14**, 7314–7328. https://doi.org/10.1039/D3RA08878B (2024).
73. Lee, J., Lee, E. J., Hwang, T. Y., Kim, J. & Choa, Y. H. Anisotropic characteristics and improved magnetic performance of Ca–La–Co-substituted strontium hexaferrite nanomagnets. *Sci. Rep.* **10**, 15929. https://doi.org/10.1038/s41598-020-72608-0 (2020).
74. Chauhan, C. C. et al. Structural, magnetic and dielectric properties of Co-Zr substituted M-type calcium hexagonal ferrite nanoparticles in the presence of α-Fe2O3 phase. *Ceram. Int.* **44**, 17812–17823. https://doi.org/10.1016/j.ceramint.2018.06.249 (2018).
75. Sedrati, C., Alleg, S., Boussafel, H. & Bendali Hacine, A. Structure and magnetic properties of nickel ferrites synthesized by a facile co-precipitation method: effect of the Fe/Ni ratio. *J. Mater. Sci.: Mater. Electron.* **32**, 24548–24559. https://doi.org/10.1007/s10854-021-06932-0 (2021).
76. Kale, A., Gubbala, S. & Misra, R. D. Magnetic behavior of nanocrystalline nickel ferrite synthesized by the reverse micelle technique. *J. Magn. Magn. Mater.* **277**, 350–358. https://doi.org/10.1016/j.jmmm.2003.11.015 (2004).
77. Aftabi, A., Tehranchi, M. M., Yusupov, R., Gabbasov, B. & Nikitin, S. Magnetic anisotropies and its optical manipulation in epitaxial bismuth ferrite/ferromagnet heterostructure. *J. Magn. Magn. Mater.* **462**, 160–166. https://doi.org/10.1016/j.jmmm.2018.04.053 (2018).
78. Aftabi, A. & Tehranchi, M. M. Optically-induced changes in magnetic properties of Fe2B/BiFeO3 heterostructure. *J. Alloys Compd.* **766**, 1054–1060. https://doi.org/10.1016/j.jallcom.2018.06.341 (2018).
79. Massoudi, J. et al. Magnetic and spectroscopic properties of Ni–Zn–Al ferrite spinel: from the nanoscale to microscale. *RSC Adv.* **10**, 34556–34580. https://doi.org/10.1039/D0RA05522K (2020).
80. Thanh, N. K. et al. Cation distribution in CuFe2O4 nanoparticles: effects of Ni doping on magnetic properties. *J. Appl. Phys.* **120**, 142115. https://doi.org/10.1063/1.4961722 (2016).
81. Shaterabadi, Z., Nabiyouni, G. & Soleymani, M. Correlation between effects of the particle size and magnetic field strength on the magnetic hyperthermia efficiency of dextran-coated magnetite nanoparticles. *Mater. Sci. Engineering: C.* **117**, 111274. https://doi.org/10.1016/j.msec.2020.111274 (2020).
82. Umut, E., Coşkun, M., Pineider, F., Berti, D. & Güngüneş, H. Nickel ferrite nanoparticles for simultaneous use in magnetic resonance imaging and magnetic fluid hyperthermia. *J. Colloid Interface Sci.* **550**, 199–209. https://doi.org/10.1016/j.jcis.2019.04.092 (2019).
83. Phalake, S. S. et al. Application of MnxFe1–xFe2O4 (x = 0–1) nanoparticles in magnetic fluid hyperthermia: correlation with cation distribution and magnetostructural properties. *ACS Omega.* **7**, 44187–44198. https://doi.org/10.1021/acsomega.2c05651 (2022).
84. Kallumadil, M. et al. Suitability of commercial colloids for magnetic hyperthermia. *J. Magn. Magn. Mater.* **321**, 1509–1513. https://doi.org/10.1016/j.jmmm.2009.02.075 (2009).
85. Lanier, O. L. et al. Evaluation of magnetic nanoparticles for magnetic fluid hyperthermia. *Int. J. Hyperth.* **36**, 686–700. https://doi.org/10.1080/02656736.2019.1628313 (2019).
86. Dennis, C. L. & Ivkov, R. Physics of heat generation using magnetic nanoparticles for hyperthermia. *Int. J. Hyperth.* **29**, 715–729. https://doi.org/10.3109/02656736.2013.836758 (2013).
87. Coffey, W. T. & Kalmykov, Y. P. Thermal fluctuations of magnetic nanoparticles: Fifty years after brown. *J. Appl. Phys.* **112** https://doi.org/10.1063/1.4754272 (2012).
88. Perrin, J. Molecular agitation and the brownian movement. *CRAS* **146**, 967–970 (1908).
89. Torres, T. E. et al. The relevance of brownian relaxation as a power absorption mechanism in magnetic hyperthermia. *Sci. Rep.* **9**, 3992. https://doi.org/10.1038/s41598-019-40341-y (2019).

Author contributions

Ali Aftabi: Conceptualization, Methodology, Software, Formal analysis, Investigation, Resources, Writing – original draft, Visualization, Writing – review & editing, supervision.Asra Babakhani: Methodology, Investigation, Resources.Roholah Khoshlahni: Formal analysis, Resources, Writing – review & editing.

Declarations

Competing interests

The authors declare no competing interests.

Additional information

Correspondence and requests for materials should be addressed to A.A.

Reprints and permissions information is available at www.nature.com/reprints.

Publisher's note Springer Nature remains neutral with regard to jurisdictional claims in published maps and institutional affiliations.